



Grain-size-reducing- and mass-gaining processes in different hydrothermal fault rocks

Alfons Berger  and Marco Herwegh 

Institute of Geological Sciences, University of Bern, Baltzerstrasse 1+3, CH-3012 Bern, Switzerland

Original Article

Cite this article: Berger A and Herwegh M (2023) Grain-size-reducing- and mass-gaining processes in different hydrothermal fault rocks. *Geological Magazine* **159**: 2219–2237. <https://doi.org/10.1017/S0016756822000218>

Received: 6 October 2021

Revised: 3 March 2022

Accepted: 3 March 2022

First published online: 16 May 2022

Keywords:

healing; PSD; fault rock chemistry; fault rock comminution

Author for correspondence:

A Berger, Email: alfons.berger@geo.unibe.ch

Abstract

Interactions of hydrothermal and deformation processes in active fault zones are important in light of seismic and geothermal activities. This study investigates different tectonites of the Grimselpass breccia fault, a hydrothermally active strike-slip structure in the Central Alps (Switzerland). We combine microstructural and geochemical investigations to decipher the interaction of grain-size reduction and associated dilation (volume gain) during frictional deformation with geochemical processes such as mass gain via precipitation, grain growth and healing. Three types of tectonites were investigated in the fault zone: (1) cockade-bearing tectonites, (2) cataclasites and (3) fault gouges. They differ in terms of microstructure of clasts, mass and volume gain/loss, as well as type and degree of cementation. Clast size distributions show decreasing median values from low-strain cataclasites to high-strain cataclasites. Mass/volume gains are up to 20 %, with samples of smallest clast sizes often showing the highest mass gain. In the case of cockade-bearing tectonites large volume and mass gain occur. In particular, the precipitation of SiO₂-rich cements is inferred to (i) reduce permeability and (ii) induce a gain in strength of the respective fault rocks. Location, timing and degree of healing directly control the fault architecture by deactivating fault strands from the circulation of hydrothermal fluids. In this case, new rupturing events are necessary to reactivate locked fault strands. Such feedback cycles of episodic deformation, mass/volume and clogging preserved hydrothermal circulation and deformation over the last 3.4 Ma, representing a process chain for the long-term preservation of orogenic hydrothermal systems.

1. Introduction

Frictional behaviour represents the dominant deformation style in upper crustal basement rocks including a variety of deformation processes (e.g. Handy *et al.* 2007; Faulkner *et al.* 2010; Cox, 2010; Fossen & Cavalcante, 2017 and literature therein). In this light, faults have been investigated in terms of their bulk mechanical behaviour using experiments and studies on natural examples (e.g. Bos & Spiers, 2000; Storti *et al.* 2003; Tenthorey *et al.* 2003; Nakatan & Scholz, 2004; Niemeijer & Spiers, 2006; Tenthorey & Cox, 2006; Keulen *et al.* 2007, 2008; Caine *et al.* 2010; Niemeijer *et al.* 2010). To understand the deformational behaviour of bulk aggregates, knowledge on the effect of local microstructural processes and their changes in space and time is required. In particular, local variations in the type of deformation and associated tectonites will influence fluid flow, dissolution, mass transfer and healing (precipitation). Numerous studies have demonstrated losses in host rock strengths by progressive embrittlement, leading to grain-size reduction and dilatation, which enhances permeability and promotes local dissolution and mineral precipitation (e.g. Chester & Logan, 1986; Bruhn *et al.* 1994; Evans & Chester, 1995; Caine *et al.* 1996, 2010; Evans *et al.* 1997; Keulen *et al.* 2007, 2008; Micklethwaite, 2009; Niemeijer *et al.* 2010, Stünitz *et al.* 2010; Hausegger & Kurz, 2013; Melosh *et al.* 2014, 2016; Carpenter *et al.* 2016; Rowe *et al.* 2019; Hooker & Fisher, 2021; Williams *et al.* 2021). As a consequence of the latter, the strength of the fault rocks increases again, requiring a new stage of embrittlement for further progressive deformation. Such healing–deformation cycles are of particular importance for the change between fast fracturing processes versus slow cataclastic flow (e.g. Micklethwaite & Cox, 2004; Cox *et al.* 2021). Healing/cementation processes and their effect on permeability/compaction have been intensely investigated in the case of sedimentary rocks undergoing diagenesis (Laubach *et al.* 2010 and literature therein), and several examples in continental basement rocks (e.g. Kerrich *et al.* 1980; Evans & Chester, 1995; Williams *et al.* 2021). In this study we aim to close this gap by investigating granitoid host rocks undergoing brittle deformation within a hydrothermal environment.

The investigations on these brittlely deformed fault rocks require application of a field-based nomenclature (e.g. Sibson, 1977; White, 1982; Wise *et al.* 1984; Chester *et al.* 1985; Schmid & Handy, 1991; Jebrak, 1997; Woodcock & Mort, 2008; Rowe & Griffith, 2015). Depending on the degree of deformation and the amount of matrix and embedded clasts, expressed as volumetric ratio, cohesive fault rocks are discriminated into breccias and (proto- to ultra-)cataclasites, while non-cohesive fine-grained fault rocks are often referred to as fault-gouge (e.g. Sibson, 1977;

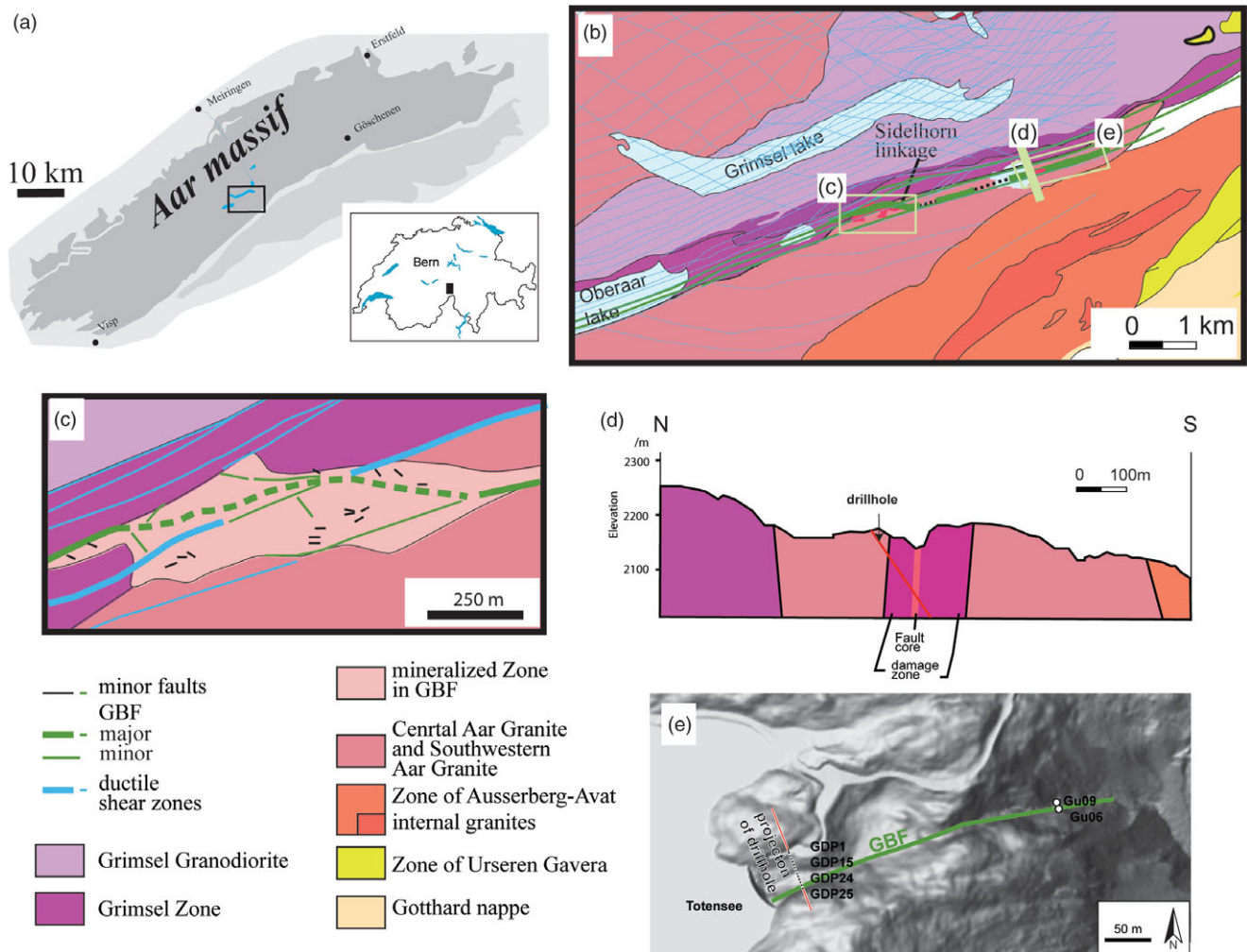


Fig. 1. Geological situation of the Grimsel area. (a) Overview of the geological setting in the central southern Aar Massif; (b) geological map of the Grimsel breccia fault; (c) detail of the Sidelhorn linkage zone; (d) tectonic cross-section through the Grimsel breccia fault in the Totensee area (see (b) for section trace); (e) hillshade of the Totensee area (www.map.geo.admin.ch: Federal Office of Topography swisstopo) with the location of the drillhole trace and locations of most of the used samples (after Belgrano *et al.* 2016; Berger *et al.* 2016; Wehrens *et al.* 2017; Egli *et al.* 2018).

Schmid & Handy, 1991). Additionally, clast-size-dependencies, such as 'small' and 'large', have been used to further discriminate and categorize fault rocks in the field (Woodcock & Mort, 2008; Luther *et al.* 2013). Special cases of fault-related rocks are cockade-bearing tectonites (e.g. Berger & Herwegh, 2019; Masoch *et al.* 2019). In examples of cockade cores completely surrounded in 3D by concentric hydrothermal growth zonation, the aforementioned studies connected the cockade growth to earthquakes. It is important to note that this tectonite type requires large fluid volumes and precipitation that form these characteristic hydrothermal growth textures.

In this study, we particularly focus on highly deformed brittle fault rocks, i.e. cataclasites, and discuss the role of different processes involved during their formation. We connect deformation microstructures to their chemical evolution. The clast microstructures are quantified in terms of particle size distribution (PSD; e.g. Sammis *et al.* 1986, 1987; Turcotte, 1986; Heilbronner & Keulen, 2006). In addition, the chemical variations between the different fault rocks are investigated in order to quantify the role of mass transfer. The link between microstructural observations and chemical data is of special interest for the investigated

Grimselpass fault zone, because cataclasites are closely linked to the occurrence of cockade-bearing tectonites, the latter representing evidences for seismic rupturing (Berger & Herwegh, 2019).

2. Geological setting

We investigate the Grimsel breccia fault (GBF; Fig. 1), a brittle structure within the several tens of km long crustal-scale Grimselpass fault zone (Belgrano *et al.* 2016; Wehrens *et al.* 2016, 2017; Herwegh *et al.* 2020). Deformation of the Grimselpass fault zone localized along the lithological boundaries of the Grimsel Granodiorite in the north block and the Southwestern Aar Granite in the south block, sandwiching locally in between the Grimsel zone (gneisses, granitoids and meta-sediments) (Fig. 1; Stalder, 1964; Niggli, unpubl. PhD thesis, Univ. Bern, 1965; Pfeifer *et al.* 1992; A Pochon, unpub. Diploma thesis, Univ. Neuchâtel, 1997; Hofmann *et al.* 2004; Belgrano *et al.* 2016; Egli *et al.* 2018). The nowadays exhumed parts of the Grimselpass fault zone and its sub-recent brittle reactivation evolved over a timespan of more than 20 Ma under different kinematic regimes and at different crustal levels. The initial shear

zones evolved under dominantly ductile deformation conditions at depths of *c.* 20 km and temperatures of 450 °C. However, they show already at that crustal level evidences for intercalation of aseismic and seismic deformation (Wehrens *et al.* 2016). Exhumation, progressive cooling and embrittlement of the fault zone yielded strong strain localization in the form of the GBF, a brittle strand within the wider former Grimselpass shear zone. This fault zone differs from other brittle structures in the area by its distinctive, long-lived hydrothermal activity, and still active sub-thermal water flow (Hofmann *et al.* 2004; Rolland *et al.* 2009; Belgrano *et al.* 2016; Wehrens *et al.* 2016, 2017; Diamond *et al.* 2018). In this study, we mainly investigated cataclasites, which are located inside the Southwestern Aare Granite. In addition, shear fractures with different offsets and tensile fractures are numerous (Belgrano *et al.* 2016; Egli *et al.* 2018). The rare kinematic indicators of the brittle deformation indicate dextral strike-slip fault kinematics (Belgrano *et al.* 2016), which is in line with the regionally observed dextral transpression along the rim of the Southern Central to Western Aar Massif (Herwegh *et al.* 2020). In terms of fault zone architecture, linkage zones and structural bridges occur on different scales (mm to hundreds of metres), playing an important role for both deformation and hydrothermal fluid flux (Belgrano *et al.* 2016).

On the metre- to kilometre scale, the GBF and its ductile precursor shear zone strands have been mapped in detail (Fig. 1; Belgrano *et al.* 2016; Wehrens *et al.* 2017). In terms of field appearance, the GBF can be divided into core tectonites, surrounding fractures in the damage zone and a mineralized zone consisting of fracture-bound hydrothermal precipitates (Hofmann *et al.* 2004; Belgrano *et al.* 2016). Meso- and micro-structural observations indicate multiple brecciation events (Hofmann *et al.* 2004; Berger & Herwegh, 2019). The appearance of the cataclasites in the fault cores varies already macroscopically by their colour, mineralogy and clast sizes. Hydrothermal activity started at the latest at 3.4 Ma (Hofmann *et al.* 2004), and episodically continued to the present day as evidenced by hydrothermal apatites (Berger *et al.* 2022) and present-day subthermal springs (Pfeifer *et al.* 1992; Waber *et al.* 2017; Diamond *et al.* 2018; Wanner *et al.* 2019). Fluid inclusion studies in hydrothermal SiO₂ precipitates indicate a main hydrothermal overgrowth between 100 °C and 160 °C (Hofmann *et al.* 2004). Besides surface outcrops and samples, we also build on samples and data from a research drilling project which hit the GBF at depths of ~30 m (for details see Egli *et al.* 2018; see also Fig. 1e). A great benefit of the drilling is that it allows sampling of fault gouges, which are mostly washed out at the surface and are therefore no longer accessible.

3. Methods

3.a. Bulk and mineral chemistry

Inductively coupled plasma emission spectroscopy and inductively coupled plasma mass spectrometry techniques are applied for bulk rock chemical analyses performed by AcmeLabs[®]. Detailed procedures can be found at www.bvna.com/mining-laboratory-services (formerly www.acmelab.com). The analytical errors of chemical data are generally <1 %. In all the diagrams presented the analytical error of bulk rock data is smaller than the symbol size in the plots. In addition, X-ray-fluorescence (XRF)-derived bulk rock data from the literature are incorporated (Schaltegger, unpubl. PhD thesis, Univ. Bern, 1989; A Pochon, unpub. Diploma thesis, Univ. Neuchâtel, 1997).

3.b. Methods to quantify mass/volume changes (Grant diagrams)

From a chemical point of view, possible mass and/or volume gain can be discussed in different ways (Gresens, 1967; Grant, 1986, 2005). Grant (1986) gave an overview for potential mass changes during alteration of rocks. In this approach, potential geochemical mass changes are unravelled by comparing concentrations of a mobile with an assumed immobile element. This results in:

$$(\Delta C_i/C_i) = (C_j^A/C_j^C)(C_i^A/C_i^C) - 1 \quad (1)$$

The assumption of a constant mass yields

$$(\Delta C_i/C_i) = (C_i^A/C_i^C) - 1 \quad (2)$$

or for constant volume

$$(\Delta C_i/C_i) = (\rho^A/\rho^C)(C_i^A/C_i^C) - 1 \quad (3)$$

where C^A and C^C are the concentrations of the starting material and the altered rock, respectively. Constants ρ^A and ρ^C represent the densities of starting and altered material. Subscripts *i* and *j* stand for an immobile and mobile element, respectively. Note that all three assumptions can be problematic, having often been the subject of multiple mass transports events. Conservation in volume requires closed systems, which also might not hold in the case of a hydrothermal system. Because of these substantial uncertainties in Equations (2) and (3), we mainly restrict our analysis to the assumption of immobile elements. This assumption is difficult to prove for major elements, which are highly dependent on the masses and volumes involved. Trace elements provide a way out of this dilemma since they are less dependent on mass or volume changes (e.g. Marquer, 1989). We therefore apply the trace element approach (Equation (1)) to detect and compare potential mass or volume gain between the different tectonites.

3.c. Particle size distribution (PSD)

In the past, different methods have been used to estimate PSD (see Table 1; Keulen *et al.* 2007, their table 1). In non-cohesive materials, the most efficient approach to obtain quantitative information on grain-size fractions is sieving and weighting, which primarily results in mass against particle size information (e.g. Anderson *et al.* 1983). As a first approach of this study, sieving is used for grain-size estimates of primary non-cohesive material, i.e. for fault gouges. They are sieved under wet conditions through mesh apertures of 16.0, 8.0, 4.0, 3.327, 2.367, 1.397, 1.0, 0.5, 0.25 and 0.125 mm. After each sieving step, the dried residue was weighted and recorded. The measured mass can be transferred into a volume by using an assumed average density (2.65 g cm⁻³) of the particles. However, such bulk volume estimates are not directly comparable with particle size frequency data as they result from other methods. Therefore, we transformed the obtained volumetric information into particle size estimates. We used the first-order assumption of spherically shaped particles, with a specific particle diameter obtained for each mesh interval, allowing the calculation of the volume of one average-sized particle. The number of equivalent spherical grains was then determined by dividing the bulk volume by the volume of the average particle size.

The second approach for particle size estimation is based on quantitative image analysis, which is applied on thin-sections of cemented cataclasites. Micro-photographs acquired by scanning

Table 1. Review of PSD data

Reference	Rock type	$d_{\min}/\mu\text{m}$	D	Location	Method	Remarks
Breccias in granitoid rocks						
Sammis <i>et al.</i> (1986)	Granite	2	1.6	Lopez Canyon	LM, SEM	
Blenkinsop (1991)	Granite, gneiss	3	1.9–3.0	SAF Canyon pass	LM	
Blenkinsop (1991)	Breccia/gouge	8	2.1–5.5	San Gabriel	LM	Different protoliths
Sammis <i>et al.</i> (1986); An & Sammis (1994)	Granite	2	1.4–2.6	SAF Tejon pass	S, LPS	
Sammis <i>et al.</i> (1986); An & Sammis (1994)	Gneiss	2	1.6–1.9	San Gabriel	S, LPS	
Sammis <i>et al.</i> (1986); An & Sammis (1994)	Tonalite	2	1.5–1.9	Lopez Canyon	S, LPS	
Shao & Zou (1996)	Gneiss	6	1.6	Qinling Mountain	LM, SEM	
Monzawa & Otsuki (2003)	Granite	10	1.7	Tanakura	LM	
Monzawa & Otsuki (2003)	Granite	11	2.1	It.-Shimotsutaki	LM	
Monzawa & Otsuki (2003)	Granite	7.7	2.2–2.6	Nojima	LM	
Chester <i>et al.</i> (2005)	Granite	0.05	2	SAF Punchbowl	LM, TEM	
Heilbronner & Keulen (2006)	Granite	0.03	1.6–2.4	Nojima	DIA	Two PSD fractions per sample
Keulen <i>et al.</i> (2008)	Granite	0.03	1.6–1.7	Black Forest	DIA	Two PSDs
Molnar <i>et al.</i> (2014)	Cataclasites, breccia		1.0–2.7	Basement, Pannonian basin	DIA	
Luther <i>et al.</i> (2013)	Cataclasites		2.6–3.5	West Salton; Whipple faults	DIA	
Pulverized granite						
Wilson <i>et al.</i> (2005); Rockwell <i>et al.</i> (2009); Wechsler <i>et al.</i> (2011)	Pulverized granitoid	0.03	2.5–3.1	SAF, Tejon granite	S, LPS	Two PSD fractions per sample
Carbonate						
See summary in	Carbonate		2.0–3.5	Carbonate faults	All	New methods applied
Cortinovis <i>et al.</i> (2019)						
Granitoid rocks						
Haines <i>et al.</i> (2013)	Gouge/experimental	~8	2.6–3.0			
Stünitz <i>et al.</i> (2010)	Experimental	0.01	1.0–2.2			
Jebrak (1997)	Breccia/gouge	10	1.3–1.6	Canjon pass		
Jebrak (1997)	Breccia/gouge	1000	1.2–1.4	Abitibi		
Melosh <i>et al.</i> (2014), (2016)	Mixed	20	0.9–1.9	Pofadder shear zone	S	
Monzawa & Otsuki (2003)	Gouge	11	2.1	Koi gouge	LM	

Note: LM: light microscope; DIA: digital image analysis; SEM: Scanning electron microscope; LPS: Laser particle sizer; S: sieving.

electron microscope (SEM) or optical microscope are used to manually redraw individual particles, the particle areas of which are then analysed by the software ImageJ 1.46. Afterwards, the resulting area of each particle is transferred into a 2D equivalent circular diameter (e.g. Berger *et al.* 2011; Heilbronner & Barrett, 2014). Measurements were done on line drawings. Analysed grain numbers are between ~230 and ~800 grains per sample analysed (Table 2).

Fractal dimensions are useful to represent suitable quantitative descriptions of PSD analysed on different magnifications (Turcotte, 1986; Blenkinsop, 1991; Jebrak, 1997) and are also determined in this study. For each tectonite sample the fractal dimension (D) is estimated by (Turcotte, 1986):

$$N(d) \sim d^{-D} \quad (4)$$

where $N(d)$ is the number of particles in the size-class d , with d as diameter of the particles. The estimation of D has lower and upper limits depending on the fractal behaviour of the particles and the measurement range (Blenkinsop, 1991; Heilbronner & Keulen, 2006; Keulen *et al.* 2007; Kruhl, 2013). Several points need to be considered when dealing with PSD: (i) PSD data only reflect the grain-size range covered by the respective imaging technique. Hence larger and smaller grain-size classes beyond the image resolution are not captured (e.g. Keulen *et al.* 2008; Cortinovis *et al.* 2019). (ii) The applicability of the power law relationship of Equation (4) has been questioned (Phillips & Williams, 2021). In this sense, different uncertainties in PSD data have been suggested to result from a combination of the type and quality of the raw data and the power law relationship used (Phillips & Williams, 2021; see Supplementary Material available online at

Table 2. Data from PSD analysis

Sample		<i>N</i>	<i>d</i> _{min}	<i>d</i> _{max}	<i>d</i> _{median}	<i>D</i>	φ	Area	Method
			(mm)	(mm)	(mm)		(dc)		
GR22	Cata.	696	0.0008	0.22	0.016	3.3	0.01	0.76	DIA; LM
GDP1-2 LM	Cock.	819	0.006	2.809	0.05	2.9	0.01	0.95	DIA; LM
Gu06	Cata.	275	0.002	4.31	0.107	2.8	0.01	0.95	46 DIA; LM
Gu09	Cata.	230	0.5	30.45	2.77				4200 DIA; HS
GDP15-4	Cata./gouge					2.6	0.5	0.72	S
GDP24	Gouge					2.6	0.13	0.96	4000* S
GDP25	Gouge					2.3			4000* S

Note: Area: analysed area; Cata: cataclasite; Cock.: cockade-bearing tectonite; *D*: fractal dimension; dc: minimum clast size; DIA: digital image analysis; HS: hand sample; LM: light microscope; S: sieving. φ : see equation 5b.

<https://doi.org/10.1017/S0016756822000218>; Torabi & Berg, 2011). For example, the truncation effect (underestimation of small particles due to resolution limitations) and the censoring effect (underestimation of large particles due to the size limitation of the sampling area) will influence the reliability of any power law fit. Being aware of these basic uncertainties, we do not use the power law relationship to infer specific processes but rather apply the approach for the discrimination of our different microstructure types. Since we consistently apply the approach following previous studies, our data can also directly compare among the different datasets (Table 1). In order to clearly declare the problem of using a power law for a limited grain size range, we indicate the lower grain-size limits as additional values in our microstructural dataset.

Hadzadeh & Johnson (2003) introduced the comminution intensity, φ , as a microstructural variable:

$$\varphi = 1 - [A_{dc}/(A_0 - \varphi * A_0)] \quad (5a)$$

where A_{dc} is the total area of the particle population critical size, A_0 is the total measurement area and φ is the initial porosity. In the case of an unknown initial porosity, the equation simplifies to:

$$\varphi = 1 - A_{dc}/A_0 \quad (5b)$$

The definition of A_{dc} depends on the fractal character of the PSD. This yields, for example, an expression in the form of $\varphi = 0.9_{d_{0.1}}$, where comminution reduced 90 % of the particles to a particle size smaller than 0.1 mm.

The φ value can therefore be used as a microstructural parameter, which is identified by the clast versus matrix area ratio. A definition of a minimum clast size ('dc' in Equation (5)) will give additional information on the truncation effect, but also limit the scale of the PSD. The definition of matrix and clasts depends on the selected fault rock (Fig. 2).

4. Results

4.a. Tectonite types and their geometric relationships

We investigate the microstructures and chemistry of selected samples, which are subdivided into the following tectonite groups: (1) cataclasites (different comminution intensities), (2) cockade-bearing tectonites and (3) fault gouges (Fig. 2). Note that the geometric relationship of the block diagram schematically shown in Figure 2a holds for a variety of scales. In addition to these

tectonites, the host rock, as starting material, was also investigated in terms of chemistry. The cataclasites form different planar high-strain zones ranging from the mm to the metre scale and show a broad range of clast sizes (see below). The cockade-bearing tectonites occur only locally on the cm to dm scale within vertically oriented tube-like channels (Figs 2a, d, 3a). These channels occur inside the tectonites of the GBF (see above). These cockade-bearing rocks show still-existing open porosity (Fig. 3; see Berger & Herwegh, 2019). In many cases, the core of individual cockade particles consists of pre-existing cataclasites, which were fragmented and mobilized during cockade formation (Berger & Herwegh, 2019). Hence it is important to note that cockade formation requires dilatant brittle deformation. The cataclasites have high variability in clast volume and clast sizes. As a function of the analysed clast sizes, the cataclasites can be further discriminated (Table 1; Section 4.c).

In the study area, the spatial distribution of cataclasites shows a scale dependency (Figs 4, 5a). At first glance, the large-scale trends of cataclasites and hydrothermally altered zones (Fig. 4a) are NE-SW- to E-W-directed (Fig. 1b, c), but can be more differentiated at the tens of metres down to the metre scale (Fig. 4a, b). At the latter scale, the main cataclasite bands separate domains of 'intact' host rocks, being themselves heterogeneously dissected by localized brittle structures such as open fractures, cockade-bearing tectonites and hydrothermal alteration zones (Fig. 4). At the map view, their traces are oblique to the main cataclasites but parallel to maximum stress direction. The main cataclasites show evidence for intense multiple deformation events, as indicated by cross-cutting relationships like cataclasite clasts within cataclasites (Figs 5, 6). Also in the case of cockade-bearing tectonites, multiple overprints (e.g. cockades in cockades, cockades with cores of pre-existing cataclasites; Figs 2, 3) occur, documenting the cyclical character of deformation and precipitation in these hydrothermal fault rocks.

4.b. Starting material (Southwestern Aar Granite and mylonites)

The country rocks of the GBF are the Southwestern Aar Granite, in fact a meta-granite, and precursor mylonites (see above). Besides documenting ductile deformation stages in the Aar Massif in general and of the Grimselpass shear zone in particular, these rocks also represent the starting material of the investigated brittle fault rocks. Owing to Alpine deformational overprint, the Southwestern Aar Granite is characterized by a gneissic texture of mm-scaled feldspars (albite and K-feldspar), often dynamically recrystallized

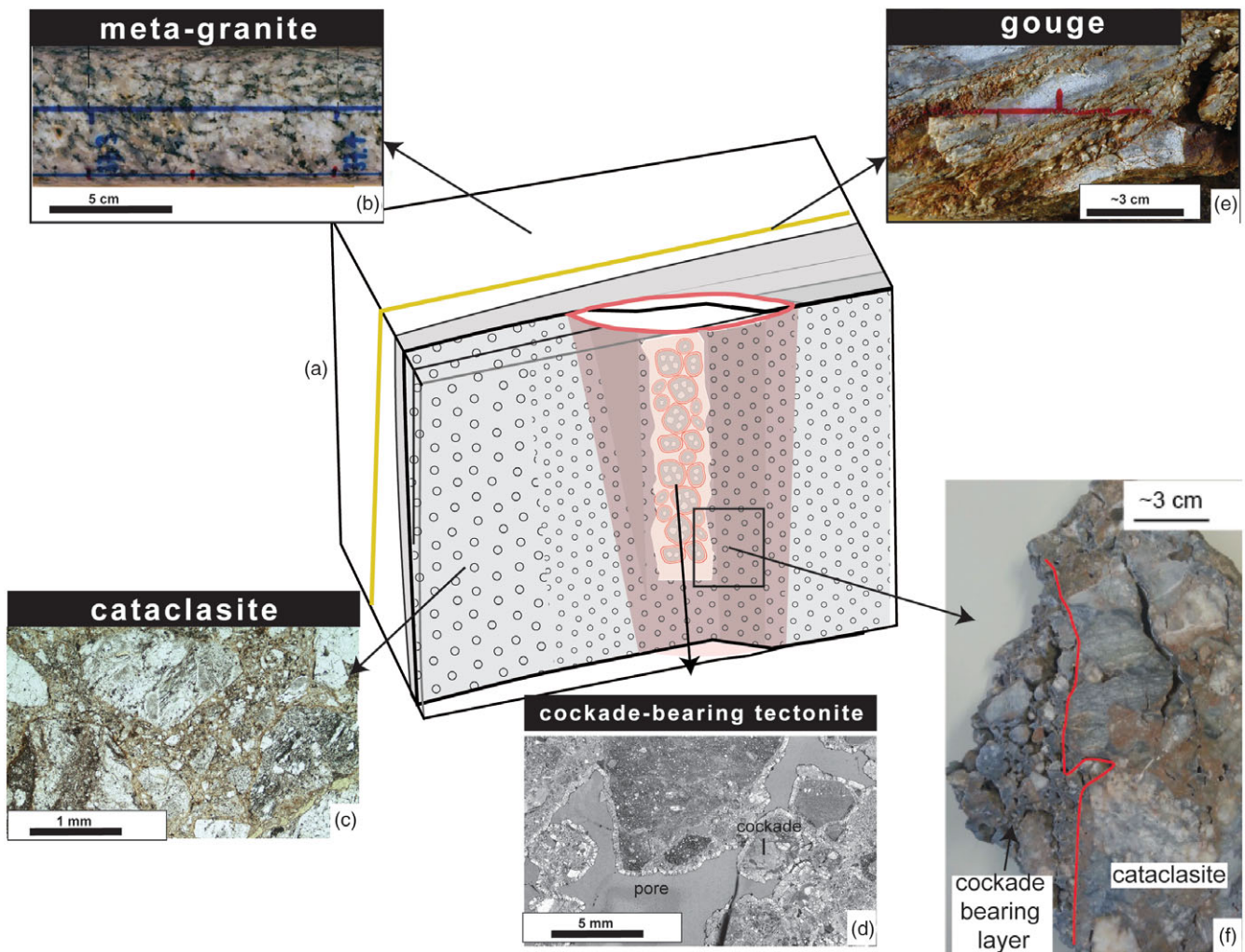


Fig. 2. Textural characterization of the different fault rocks. (a) Schematic drawing of the spatial relationships of the different tectonites (no scale). (b) Photograph of a drill core of the only weakly deformed Southwestern Aare granite. (c, d) Microphotographs (plane light) of (c) a cataclasite and (d) a cockade-bearing tectonite. (e) Photograph of a drill core of the fault gouge. (f) Hand sample of a breccia in contact with a cockade-bearing layer.

quartz, and variable amounts of white mica and biotite. The feldspars are altered into white mica, epidote and minor amounts of oxides. The biotite grains are often chloritized. The aligned micas form a well-visible planar gneissic fabric (Fig. 2b). The grain sizes of the micas are in the range 0.1–0.05 mm. The Southwestern Aar Granite has been geochemically characterized by different studies (Schaltegger, unpubl. PhD thesis, Univ. Bern, 1989; Schaltegger, 1990, and references therein; A Pochon, unpub. Diploma thesis, Univ. Neuchâtel, 1997; Table 3) indicating that mineralogical variations of the starting material are minor (Fig. 7; A Pochon, unpub. Diploma thesis, Univ. Neuchâtel, 1997). The rare-earth elements (REE) distribution of the host shows a typical granite pattern with a negative Eu anomaly (Fig. 7).

The mylonites contain similar minerals, but they are in rare cases enriched in white mica or quartz. Compared to the host granite, the grain size is already orders of magnitudes smaller (10–30 μm ; see Wehrens *et al.* 2016). The main deformation mechanism in the polymineralic mylonites is viscous granular flow, while in mylonitized quartz veins subgrain rotation recrystallization represents the dominant dynamic recrystallization process. The K-fsp and albite are fine-grained in the mylonites and not altered as in the coarse-grained granitic precursor.

4.c. Cataclasites

Cataclasites mostly overprint mylonitic or gneissic precursor structures (Rolland *et al.* 2009; Wehrens *et al.* 2016, 2017). Volumetrically they dominate within the suite of the studied brittle fault rocks. They show different degrees of comminution expressed by rather variable clast sizes ranging from centimetres down to micrometres (Figs 2, 8; Table 2). Rebrecciation of older cataclasite generations and cataclastic flow is common (Figs 3b, 6a; Hofmann *et al.* 2004; Belgrano *et al.* 2016 and figures therein).

The matrix of the different cataclasites can be characterized by (1) fine-grained host material; (2) overgrowth cements around larger clasts; (3) isolated newly precipitated crystals (often K-feldspar, oxides, sulphides and quartz); and (4) small-scale veins (Figs 5, 6). The overgrowth cements (2) are often K-fsp and in minor amounts also quartz (see arrows in Fig. 6c). Small veins (4) are frequent, documenting an interplay of brittle fracturing of a solidified cataclastic material and mineral precipitation. These veins are either filled by quartz or show polymineralic infill of quartz and oxides (Fig. 6b, d). The mineralogy of the fine-grained matrix is dominated by quartz and feldspars.

The clasts inside the cataclasites either consist of host rock (granite/mylonite) or precursor cataclasite fragments (Figs 2, 5).

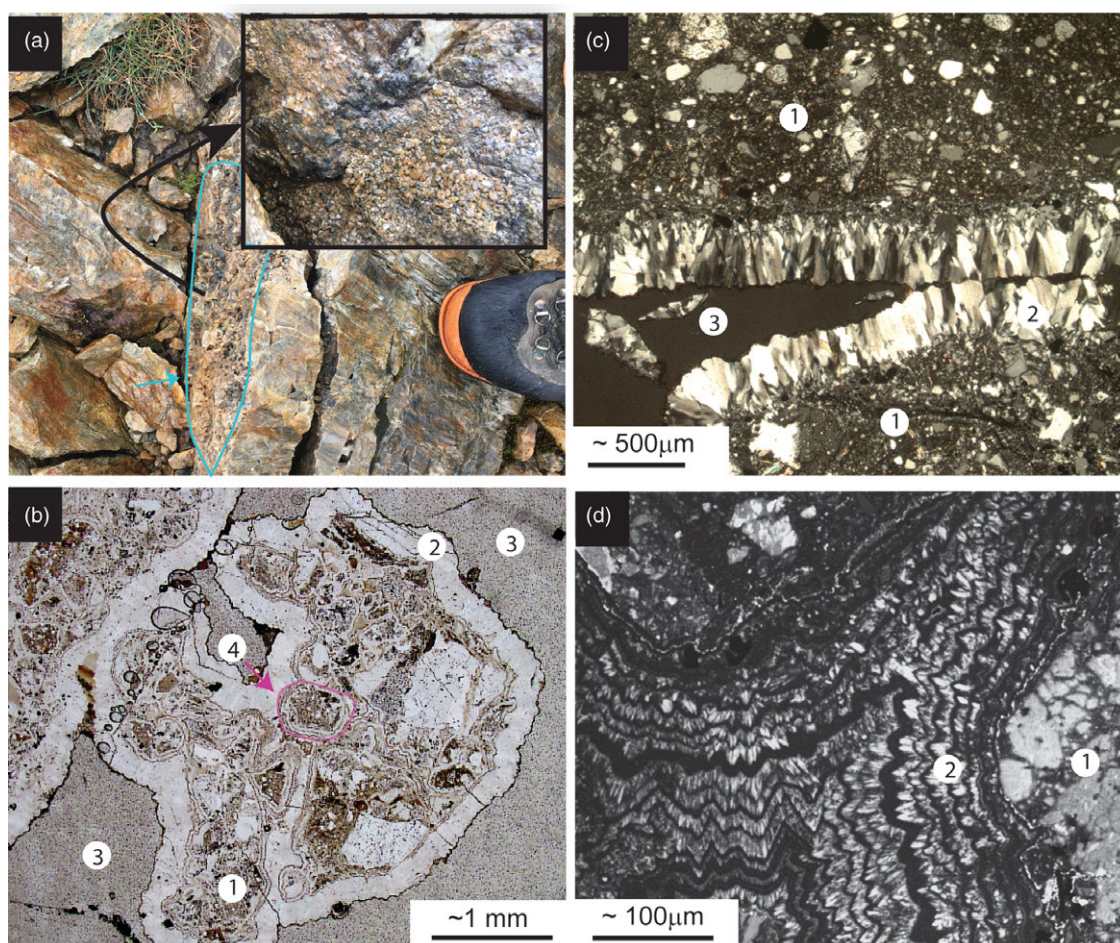


Fig. 3. Microstructures of cockade-bearing fault rocks. (a) Field photograph of a cockade tube (outlined in blue and arrow). Small inset represents the top view of this cockade tube. (b) Plane light photograph of a thin-section of a cockade-bearing tectonite. (c) Detail of a cross-polarized light photomicrograph of a cockade-bearing tectonite. (d) CL image of a detail of the cements of a cockade triple junction. Number significations in all images are: 1. cataclastic cores of cockades, 2. cockade overgrowth rim, 3. open pores, 4. cockade inside a cockade.

In the case of fine-grained clasts, the clasts preferentially are mono-mineralic (Fig. 6d, e). Depending on the clast sizes (see also ψ value in Table 2), we analysed areas from several cm^2 down to mm^2 (see Fig. 8; Table 2) to statistically properly characterize individual cataclastite types. The resulting PSDs allow for calculation of the fractal dimensions within a cataclastite, which range between 2.8 and 3.3 (Fig. 8; Table 2). Interestingly, the fractal dimension increases with decreasing clast size (see also Section 3.c and Table 1).

4.d. Cockade-bearing tectonites

Some tectonites contain cockade structures (Figs 2, 3; Berger & Herwegh, 2019). This tectonite type occurs as isolated tube-like steep channels inside the GBF (Figs 2, 3, 4). Cockade textures are usually characterized by hydrothermal precipitates around clasts (Fig. 3). These structures can only be explained by free growth of hydrothermal minerals in a fluid jet, which is also the case in the GBF (mobile cements of Berger & Herwegh, 2019; see also Masoch *et al.* 2019). The cockade layers consist of hydrothermally grown quartz (Fig. 3). Since this precipitation occurred in 3D, a floating core is necessary. This precipitation is responsible for μm -sized small growth rims around the cockade cores and related mass gain (Figs 2, 3). In addition, individual cockades can be partly cemented together mainly by chalcedony and minor

K-fsp and quartz. This cementation occurred after settling of the formerly floating cockade particles in the remaining inter-particle pore space (immobile cements of Berger & Herwegh, 2019). In rare examples, other minerals such as clay grow inside the pores. In this context, it is crucial to note that the cores of individual cockades represent the above-described cataclastites (Fig. 3). In terms of relative timing, the different layers growing around each core require the repeated occurrence of earthquakes (Fig. 3; Berger & Herwegh, 2019, chapter 6.1). Depending on the size and position of such cockade-bearing tectonites, they are overprinted either in cataclastites, or become refractured and themselves involved in a new cockade generation during a subsequent earthquake event (Fig. 3).

4.e. Fault gouges

Mechanically, the main difference between the cataclastites and the fault gouges is the missing cohesion (Sibson, 1977). The preserved fault gouges in the drill core show widths on the scale of mm to several cm (Fig. 2e). The gouge material for the PSD analysis has been scratched out between relatively intact host rock walls. Owing to this procedure, nonetheless, larger fragments of incompletely fragmented host rock could have been sampled as well. Such large fragments have been excluded from further analysis. The obtained PSDs of the two analysed fault gouges yield a fractal

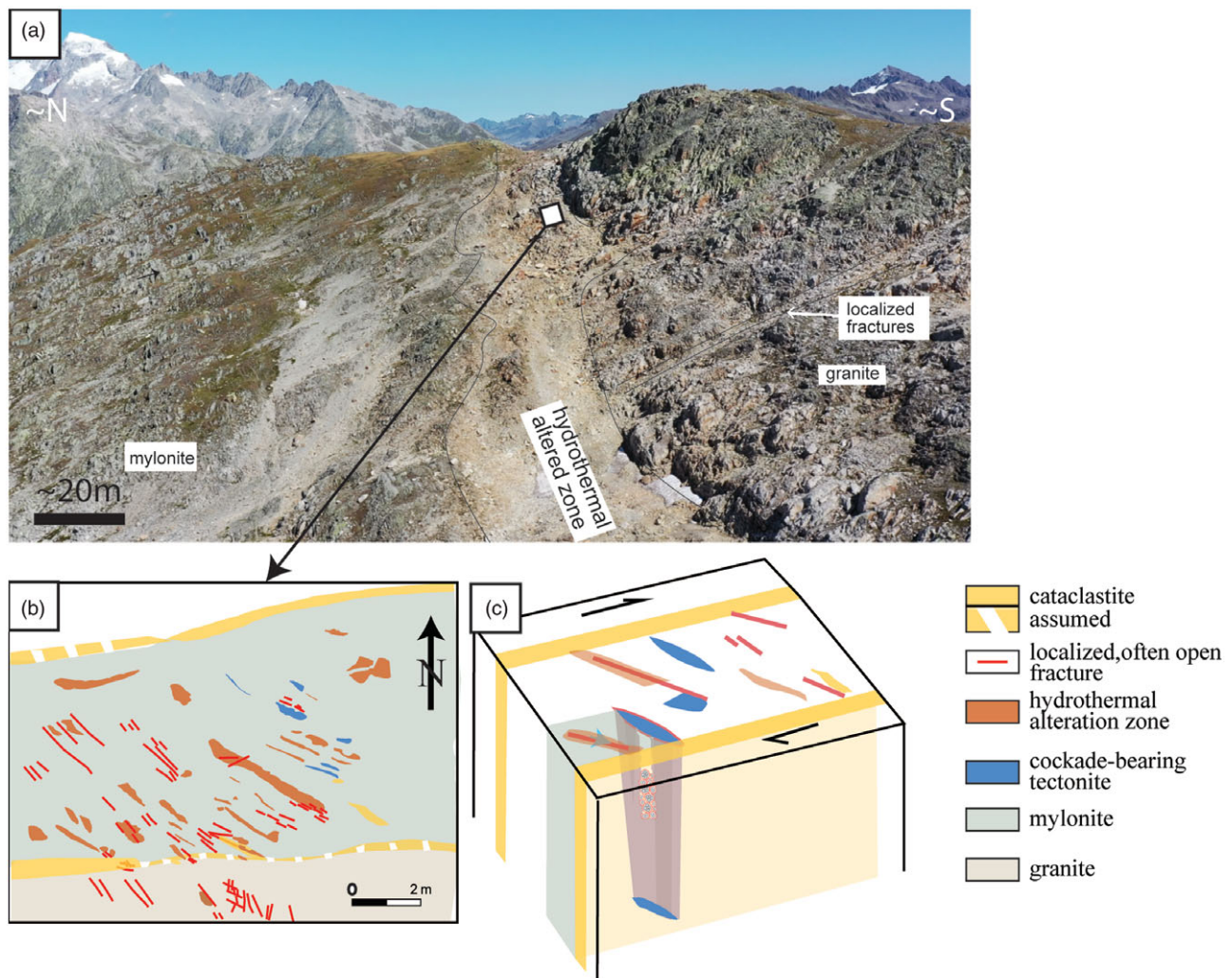


Fig. 4. Geometrical relationships between the different tectonites. (a) Drone image of a part of the Sidelhorn linkage zone. (b) Drone mapping of a small area inside (a) (an area of ~120 m²) showing the cataclasites, fractures and cockade-bearing tectonites (mapping done by C. Schmid, unpubl. Msc thesis Univ. Bern, 2021). In addition, alteration zones are mapped, which are directly linked to fractures. All structures are steep. (c) Schematic 3D sketch of the situation as mapped in (b).

dimension (D) of 2.6 (Fig. 8; Table 2). As with the cataclasites, we did not further investigate particle sizes in the fine-grained matrix, which is classified as matrix.

5. Chemistry and mass transfer

The different tectonites differ substantially in their chemistry as shown in Harker diagrams (Fig. 7). The granitic protolith and the cockade-bearing tectonites represent the two end-members in the chemical variation (Fig. 7). The chemistry of the cockade-bearing breccia is dominated by a high gain in SiO₂ (Fig. 7; Table 3). This is consistent with the observed dominant growth of hydrothermal quartz in the cockade particles (Fig. 3). The gouges show a substantial gain in Fe₂O₃, as can already be inferred from the Fe-oxides and hydroxides clearly visible in the macro- and microstructures (Fig. 6). The different cataclasites show more substantial chemical variations than the granitic host rock, particularly including chemical changes in Si, K and Na (Fig. 7).

While the Harker diagrams discussed above better illustrate the overall chemical variations between the different tectonites, the Grant analysis yields insights into mass and volume changes.

Grant diagrams allow the construction of an isocon including different immobile elements (see Section 3.b). The best-selected immobile elements in this example are Y, Ti, Zr and Th (Fig. 9). The isocon also includes Al₂O₃, indicating also relative immobile behaviour of Al₂O₃ as major element (see also Fig. 7). The immobility of Y, REE and Zr can also be seen in the constant REE pattern of the different samples. Assuming that the Y, Ti and Zr represent a useful isocon, the deviations from the 1:1 line identify elements which detect a volume gain or loss between host rock and tectonites. In a first data set, we compare a cataclasite with the protolith. Note the gain of SiO₂ and, in minor amounts, some other mobile elements (Fig. 9a). The SiO₂ not only gains in relation to the isocon, but also above the 1:1 line. This can only be explained by volume gain (see Section 3.b). This gain is variable, as seen in the Harker diagrams (Fig. 7). In a second example, we compare a gouge sample with the protolith, which shows an isocon close to the 1:1 line. With the exception of the Fe₂O₃, these samples show no large changes in mass or volume. The selected Grant diagram supports the trend already seen in the Harker diagrams (Fig. 7). In addition, it shows the different volume changes of these tectonites.

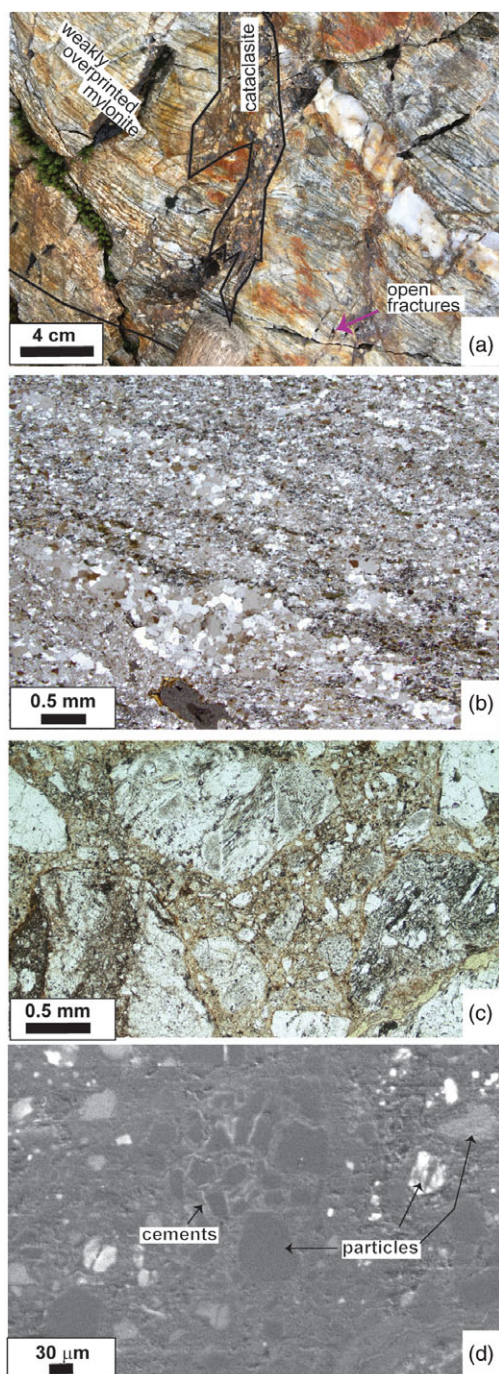


Fig. 5. Illustration of the cataclasites and mylonites. (a) Cataclasite dissecting older mylonite; (b) cross-polarized light micrograph of a quartz mylonite; (c) plane light micrograph of a cataclasite; and (d) SEM image of a cataclasite showing the K-fsp cements surrounding quartz clasts and quartz veins inside the cataclasite.

6. Discussion

As demonstrated above, the three studied end-members, cockade-bearing tectonites, cataclasites and fault gouges, show substantial microstructural and geochemical variations. In order to discuss their evolution and mechanical significance within the Grimsel breccia fault, the speed of deformation and precipitation processes represents an additional important constraint that needs to be considered. Based on our new findings and existing knowledge

from the literature, we elaborate these aspects in the following discussion, first for cockades and then for the grain-sized reduced host rock materials (cataclasites, gouges).

6.a. Processes during cockade formation

As mentioned above, the term ‘cockade structures’ is used for many spherical objects characterized by growth rims. It is a term that is especially applied in the field of ore geology (see summary in Frenzel & Woodcock, 2014). The here discussed cockade-bearing tectonites have formed by fracturing under seismic rates (Cox & Munroe, 2016; Berger & Herwegh, 2019; Masoch *et al.* 2019; see also Section 4.d, Figs 2, 3). To allow such floating cockade particles, injection of fluids at high speed into an open fracture is required. This includes fast opening and a considerable pressure drop (see Berger & Herwegh, 2019), which is only possible during earthquakes. Hence, already their appearance yields the important information of high-speed deformation and associated precipitation processes during cockade flotation in a fluid jet. Cockade growth therefore developed during and directly after seismic rupturing (Berger & Herwegh, 2019) by precipitation from an oversaturated fluid during seconds to minutes owing to a pore fluid pressure drop just after seismic rupturing. Note that the small width (<15 μm) of a growth rim and the small volumes of associated quartz precipitation require fast growth rates during the short time (minutes to hours) interval of cockade flotation. Repeated stages of fluid injection induced renewed flotation events of cockades and precipitation around cockade cores, resulting in the typical spherical growth rims (Figs 2, 3).

In contrast, the inter-particle cements represent stages of long-term precipitation within interconnected open pore space during the circulation of hydrothermal fluids between the settled cockade aggregates. This type of precipitation lasts as long as permeability is maintained before the complete clogging of the system by the hydrothermal precipitates. In the case of cockades of the GBF, estimates by Berger and Herwegh (2019) yield time intervals for this type of precipitation of hundreds to thousands of years, pointing to a slow growth of immobile cements during interseismic periods. Despite these severe differences in precipitation times, both mobile and immobile cements explain the extreme SiO₂-rich bulk rock compositions of the cockade-bearing tectonites (Fig. 7). The inferred gain in SiO₂ in combination with the extreme high porosity of these cockade-bearing tectonites relates to the volume gain by the dilatational deformation necessary for the formation of such fault rocks. In this sense, volume and mass gain is most pronounced in the case of cockade-bearing tectonites (Figs 7, 9), the reason for which is threefold: (i) substantial opening of new fracture space during one rupturing event; (ii) complete or partial filling of this pore space during interseismic mineral precipitation; (iii) repetitive cycles of (i) and (ii) during subsequent earthquake activity. Depending on the amount of quartz cement precipitation, immobile cockade cements result in a progressive gain in cohesion, i.e. a gain in rock strength with increasing amount of precipitated cement. This has important consequences for the loading stage of a seismic cycle as discussed further below.

6.b. Processes during cataclastic flow

In contrast to the volume and mass gain processes in the cockade-bearing tectonites, at first glance the main microstructural characteristics in the cataclasites and the gouges are dominated by

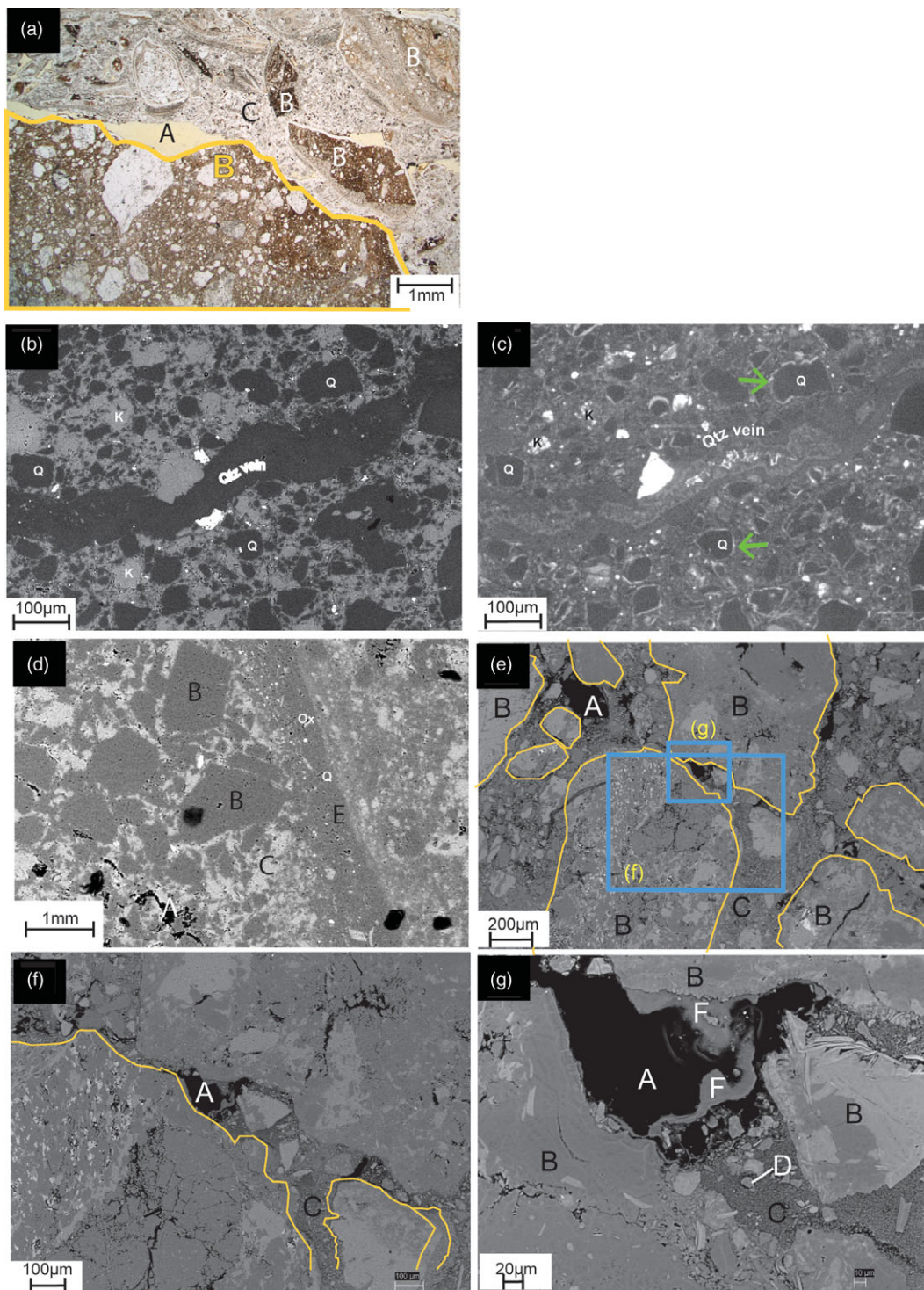


Fig. 6. Microstructures of the cataclasites. (a) Plane light microphotograph gives an overview of different generations of cataclasites and their rebrecciation. (b) Backscatter electron (BSE) image of a comminuted cataclasite being dissected by a quartz vein. (c) Same view as (b) but as CL image showing the K-fsp and quartz overgrowth of the old clasts, also illustrating the difference between old and new K-fsp and old and new quartz (see green arrows). (d) BSE image showing different clasts and the deformation features (note that the letters are explained below). (e) Overview image of a cataclasite including small and large clasts. The large clasts are outlined in yellow. The positions of images (f) and (g) are indicated. (f) and (g) are BSE images showing the different dimensions of the clast sizes and the occurrence of rock particles and newly formed minerals at different magnifications (Note particles marked with B, D and F). A: pores; B: large clasts; C: matrix with cements; D: small clasts; E: veins; F: newly precipitated mineral; Q: quartz.

progressive grain-size reduction via brittle/frictional processes. This results in the development of clast sizes covering several orders of magnitude (Figs 6, 8). While the larger particles are dominated by rock fragments, the monomineralic character of smaller

particles points to a progressive grain-size reduction and disintegration of the former host rocks. Independent of the clast sizes, clasts are always surrounded by a matrix. These matrix-dominated layers are characterized by smaller particle sizes, as previously

Table 3. Geochemical data

Sample	GDP15-02(I)	GDP15-04(I)	GDP08	GDP08 (II)	TS101	SG6	GDP15-02(II)	GDP15-02(III)	GDP15-04(II)	GDP05	SU84-35
Sample type	wr	wr	wr	wr	wr	wr	gs	gs	gs	wr	wr
Source	This study	This study	This study	This study	This study	A Pochon (unpub. Diploma thesis, Univ. Neuchâtel, 1997)	This study	This study	This study	This study	Schaltegger (1990)
Method	FUS-ICP, FUS-MS	FUS-ICP, FUS-MS	FUS-ICP, FUS-MS	FUS-ICP, FUS-MS	FUS-ICP, FUS-MS	XRF	FUS-ICP, FUS-MS	FUS-ICP, FUS-MS	FUS-ICP, FUS-MS	FUS-ICP, FUS-MS	XRF
SiO ₂	82.87	81.08	85.42	85.47	85.43	85.46	79.92	83.11	78.6	75.41	75.4
Al ₂ O ₃	8.47	9.6	7.03	6.53	6.82	6.37	10.08	8.33	10.61	13.11	12.48
Fe ₂ O ₃ (T)	1.41	1.51	1.39	2.13	1.3	2.04	1.27	1.13	1.59	1.2	1.25
MnO	0.042	0.029	0.028	0.034	0.047	0.01	0.045	0.024	0.05	0.045	0.05
MgO	0.17	0.19	0.2	0.2	0.2	0.47	0.25	0.16	0.25	0.16	0.25
CaO	0.2	0.28	0.24	0.25	0.16	0.16	0.23	0.19	0.35	0.62	0.27
Na ₂ O	1.38	1.92	0.78	0.75	0.77	0.66	1.65	1.26	1.78	3.46	3.59
K ₂ O	4.33	4.41	4.12	3.79	3.8	2.94	4.84	4.53	4.92	5.23	4.87
TiO ₂	0.082	0.096	0.066	0.063	0.07	0.15	0.109	0.081	0.12	0.106	0.13
LOI	1.06	0.85	0.81	0.87	0.89		1.37	0.82	1.42	0.47	98.33
Total	99.98	99.97	100.1	100.1	99.45	98.26	99.74	99.65	99.72	99.83	98.33
Ba	301	349	336	311	296		335	282	367	476	
Sr	48	51	40	38	39		47	41	58	67	
Y	20	22	14	14	17		21	23	22	29	
Zr	78	91	61	61	73	50	94	80	111	103	108
Cr	140	20	150	250	140		30	100	20	20	
Rb	298	269	305	273	279		354	313	325	235	
Nb	11	11	7	7	8		13	10	13	13	
La	19.7	23.1	15.1	15.5	16.5		21.8	21.5	30.4	32.3	
Ce	41.2	45.8	29.8	30.5	34.9		45.6	41.1	63.2	64.8	
Pr	4.41	4.96	3.22	3.32	3.67		4.85	4.7	6.93	7.03	
Nd	16.4	18	12.2	12.6	13.1		18.2	17.7	24.2	25.5	
Sm	3.3	3.8	2.6	2.5	2.9		3.9	4	5.3	5.4	
Eu	0.34	0.43	0.32	0.25	0.3		0.43	0.33	0.52	0.52	
Gd	3	3.3	2.3	2.3	2.7		3.3	3.5	4.3	4.7	
Tb	0.5	0.6	0.4	0.4	0.5		0.6	0.6	0.7	0.8	
Dy	3.4	3.8	2.7	2.4	3		3.8	3.7	4.3	4.8	
Ho	0.7	0.7	0.5	0.5	0.6		0.8	0.8	0.9	0.9	
Er	2.2	2.2	1.6	1.5	1.8		2.3	2.3	2.7	3	
Tm	0.33	0.37	0.28	0.27	0.31		0.4	0.39	0.42	0.47	
Yb	2.3	2.6	2	1.8	2.1		3	2.7	3.2	3.1	
Lu	0.38	0.38	0.31	0.29	0.33		0.47	0.44	0.51	0.5	

Note: Major elements in wt%, trace elements in µm/g; gs: grain size separated; WR: whole rock; Fus-ICP: Fusion-inductively coupled plasma optical emission spectroscopy; ICP_MS: inductively coupled plasma mass spectroscopy.

defined (see Equation (5)). The fractal dimension, as well as the average particle sizes, is the expression of the progressive destructive processes as a function of increasing finite strain within a non-coaxial kinematic framework.

Despite pronounced activity of destructive processes, cataclases also bear evidences for constructive processes. These are, for example, different types of grain growth in matrix grains, the occurrence of cements between matrix grains, as well as vein

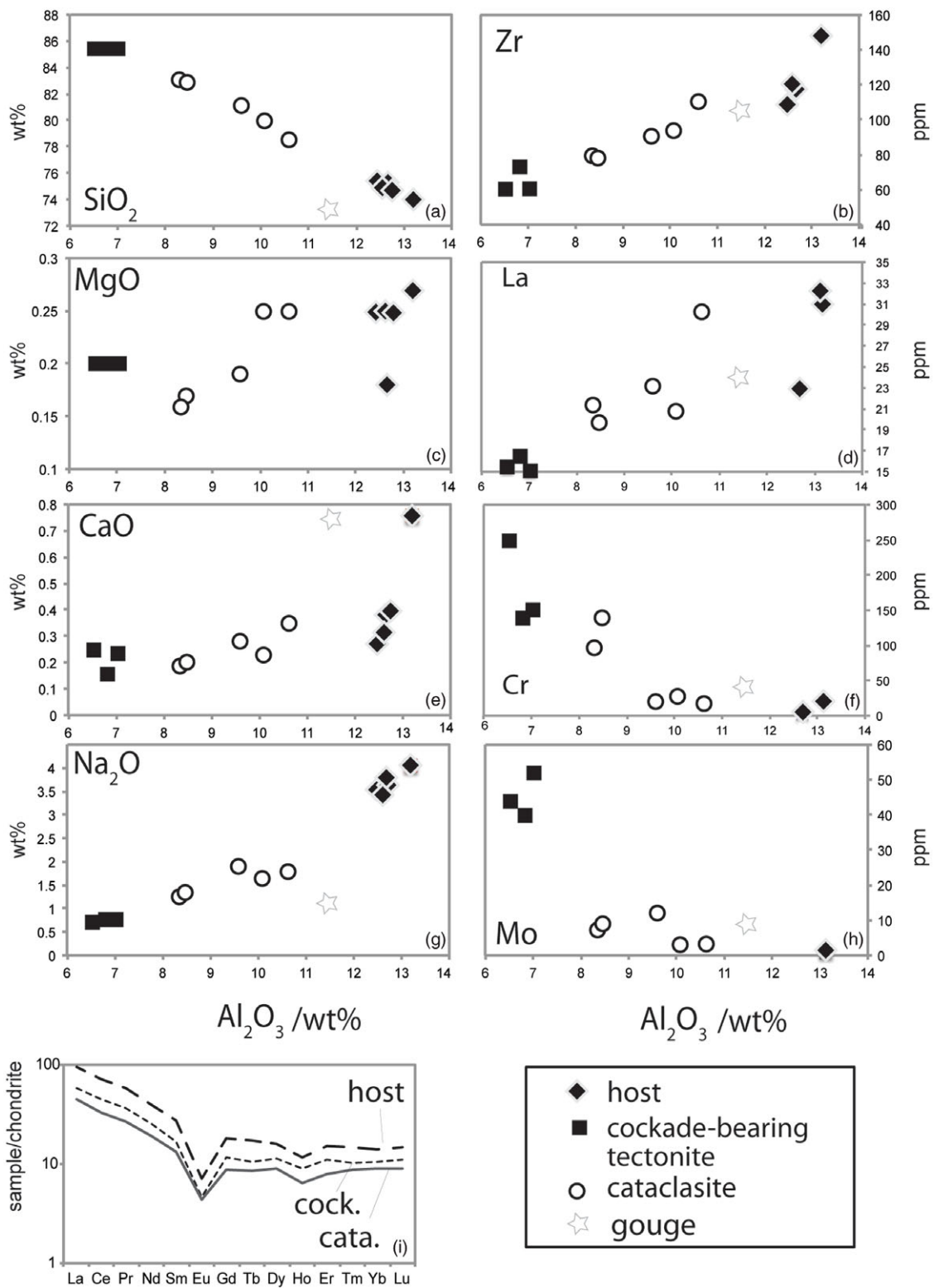


Fig. 7. Geochemical compositions of the fault rocks and related host rocks. (a–h) Selected major and trace element contents against Al_2O_3 contents. (i) REE patterns of the main elements normalized to chondrite values.

infills of fractured matrix material (different examples illustrated in Fig. 6). Similar to the constructive mobile and immobile cockade cements, also in the case of the cataclasites these processes add

mass to the system and change the mechanical behaviour, because of a gain in rock strength with increasing degree of matrix cementation. In the case of the cataclasites, we distinguish the following

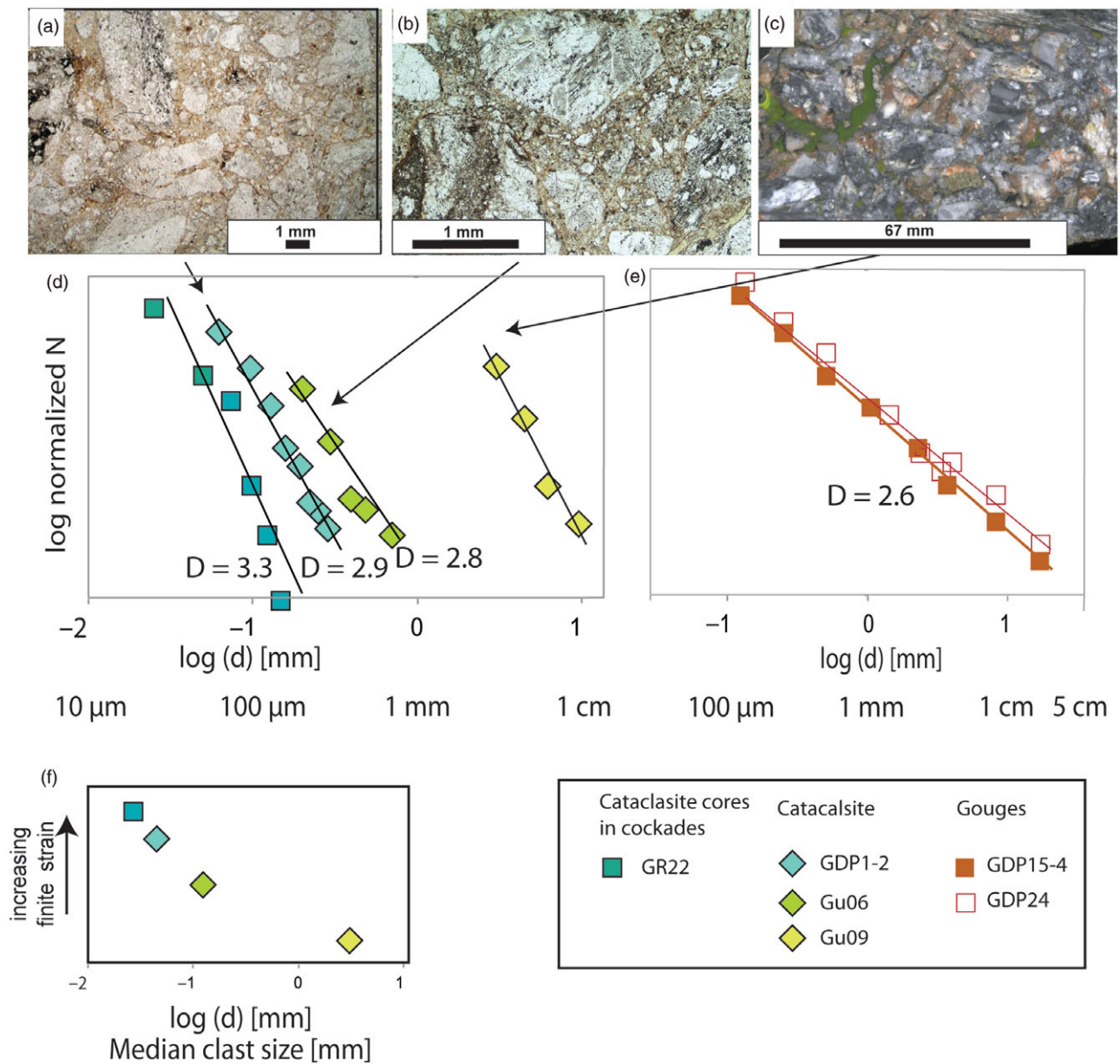
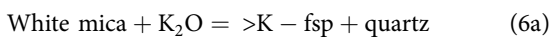


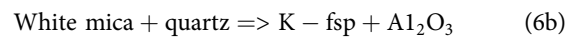
Fig. 8. Particle size distributions (PSDs) and images of the investigated samples. (a–c) Plane light microphotographs which were used for clast size analyses; (d) PSDs estimated by image analysis (sample names are indicated); (e) PSDs of gouges estimated by sieving; (f) schematic sketch of the relationship between calculated median values of the raw data versus possible change in bulk finite strain (without any scale).

types of cementation: (1) precipitation from a fluid, (2) mineral reactions forming new minerals and (3) solid reorganization by solution/precipitation.

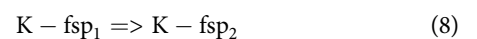
The fundamental change in chemistry and mineralogy between a fresh granitic host and the resulting cataclasite indicates the importance of K-fsp producing mineral reactions. This is consistent with the observed microstructures documenting newly formed K-fsp cements (Figs 6, 9). Hence a gain in K₂O is necessary, which leads to the reaction:



However, a local gain of Al₂O₃ cannot be excluded, which would be related to the reaction:



Based on the chemical data of this study, such a gain in Al₂O₃ is unlikely, because of the relatively constant Al₂O₃ chemistry between the different analysed tectonites (Fig. 9). Microstructural domains dominated by reaction (6a) can be recognized by the variable Al/K ratios. In addition to this mineral reaction, local dissolution, mass transfer and precipitation processes occur, which can be described as:



Reactions (7) and (8) are only visible in the cathodoluminescence (CL) images (Fig. 6c). The overall microstructures of clasts,

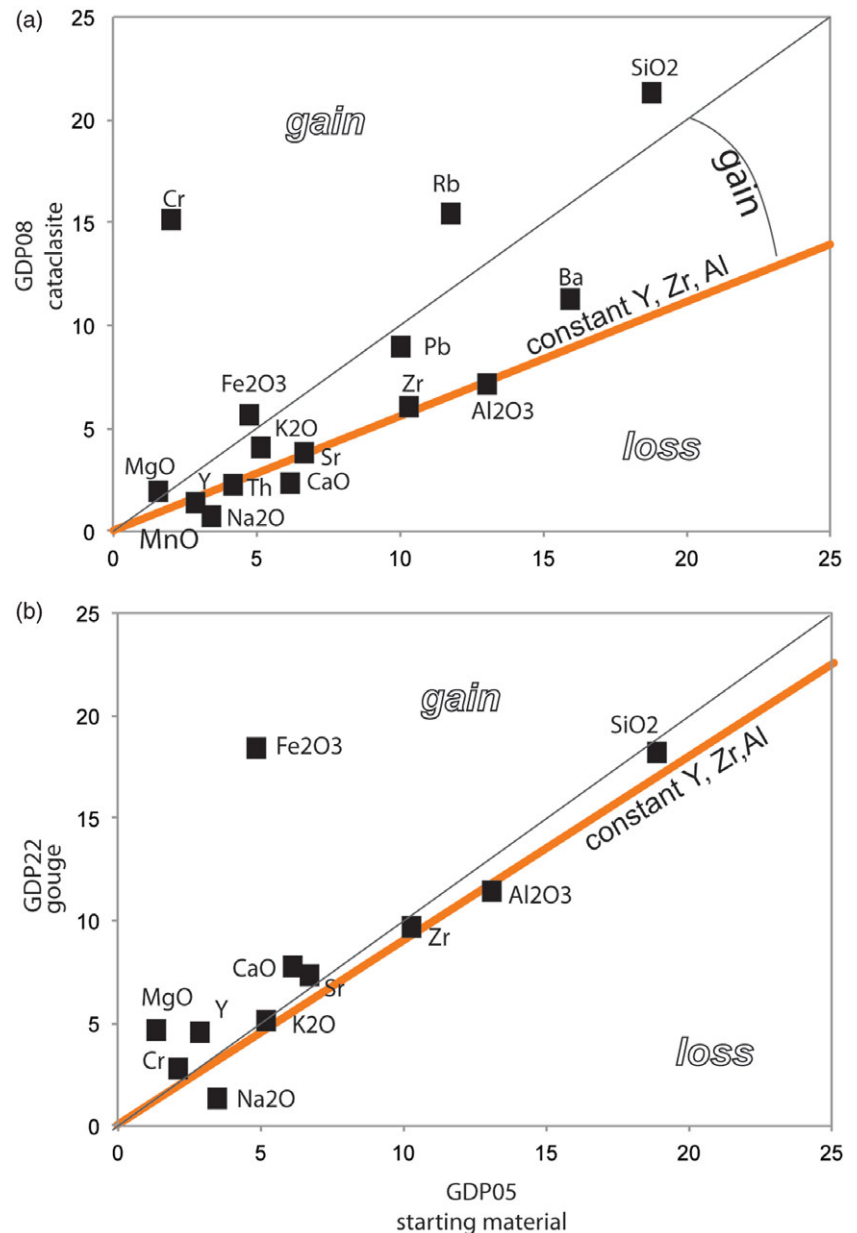


Fig. 9. Grant diagrams between the host rock (sample GDP05) and different tectonites. (a) Cataclasite (sample GDP08); (b) fault gouge (sample GDP22). Data: SiO_2 (wt %)/4, Fe_2O_3 (wt %) * 4, Al_2O_3 (wt %), MnO (wt %) * 2, MgO (wt %) * 10, CaO (wt %) * 10, Na_2O (wt %), K_2O (wt %), Ba (ppm)/30, Sr (ppm)/10, Y (ppm)/10, Zr (ppm)/10, Cr (ppm)/10, Rb (ppm)/20, Pb (ppm), Th (ppm)/5.

different types of cementation and solution/precipitation processes in the cataclasites indicate a combination of frictional deformation processes and fluid-related cementation.

Compared to the cockade-bearing tectonites, the mass gain for cataclasites is moderate (Figs 7, 9) but much more substantial than for fault gouges. In a microstructural perspective, actual locations of mass gain in the cataclastic microstructures represent the last stage of mineral precipitation in a probably long-lasting deformation history. Owing to earlier stages of cataclastic flow, earlier cement generations were destroyed either by brittle fragmentation or dissolution and renewed mobilization in the fluid. This low preservation potential of older cement generations is highly favoured by the destructive deformation processes, particularly by the aforementioned strain-dependent grain-size reduction. Vice versa, the correspondingly enhanced grain surface areas in fine-grained cataclasite matrix enhances dissolution as well as mineral reaction processes. Hence, in contrast to cockade-bearing

tectonites, the preservation of older precipitation events is rather limited for cataclasites. Only in the case of branching cataclastic bands, particularly by their deactivation owing to healing-induced gains in fault rock strength and subsequent formation of new bands, might structural witnesses survive. These structures might allow views back in time by unravelling relative sequences of deformation and healing/precipitation.

6.c. Interactions of processes

Section 6.a describes cockade-bearing tectonites, with fast-growing mobile and immobile hydrothermal cements as well as large volume and mass gain (mainly SiO_2). Section 6.b describes cataclasites with some gain of SiO_2 from a fluid and dominantly cementation including mineral reactions and precipitation. In both cases the fluids probably are identical, but their flow rates must vary owing to fault-rock-dependent changes in permeability, yielding

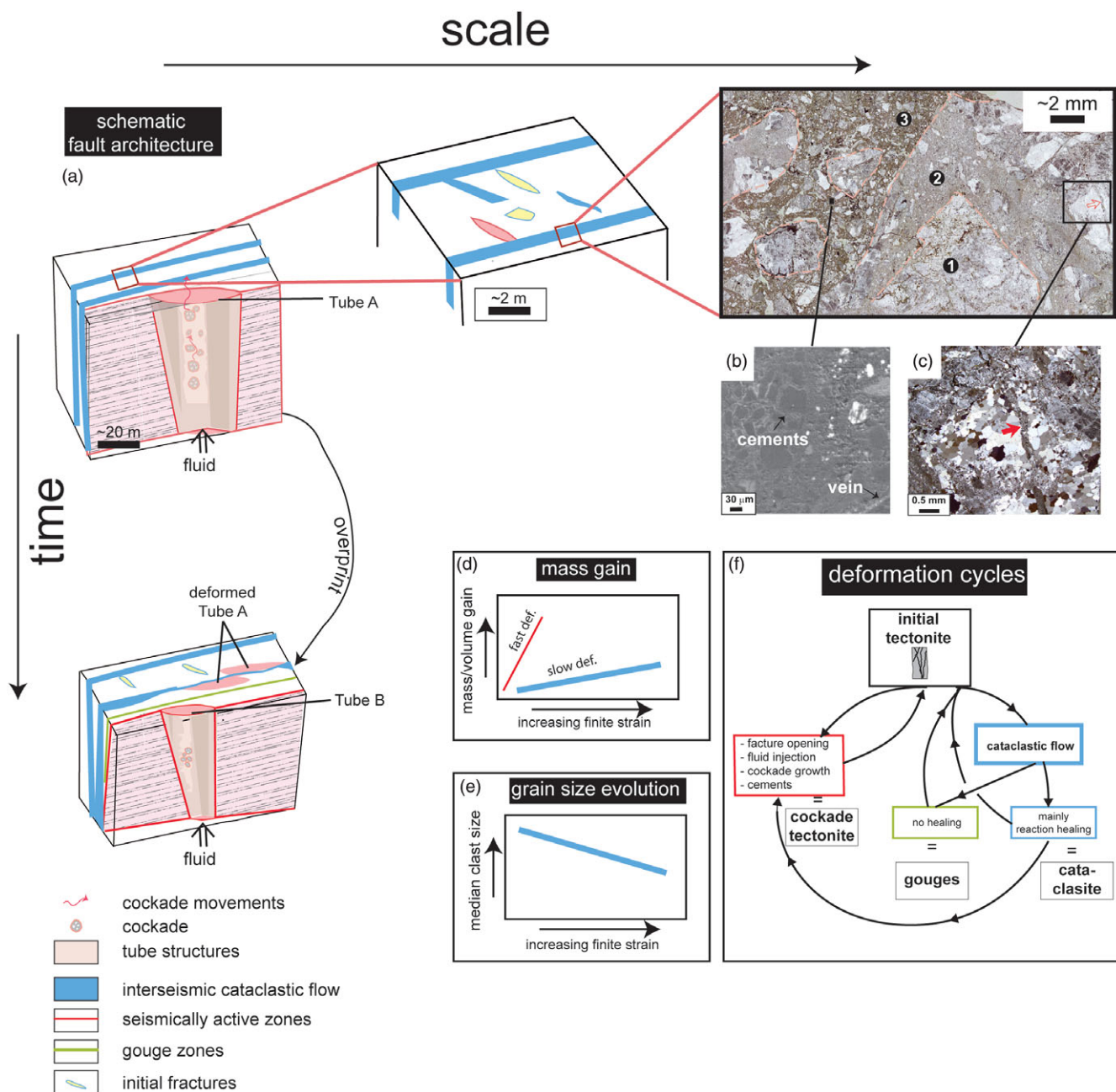


Fig. 10. Schematic overview of geometries and processes of a hydrothermal fault and their evolution in space and time. (a) Top row shows the different scales. Left column indicates the structural evolution in time showing different overprinting relationships. The overprinting of local cockade-bearing tubes is shown, but also cataclasite layers are multiply reactivated. (b, c) Details of overprinted cataclasites showing the cements and the filled fractures, respectively. (d) Schematic evolution of mass gain. (e) Clast-size evolution with increasing finite strain. (f) Summary of the cyclical interplay between grain-size reduction and precipitation for the different tectonites (cf. (a)).

differences in the aforementioned cementation behaviour. Hence, cockade-bearing tectonites and cataclasites (also gouges) must be linked and connected, in both 3D space and time. We therefore propose the following interactions:

1. The cycles of fracturing and healing influence the behaviour of fault rocks (Fig. 10f).
2. There must exist a close feedback between cycles of fracturing and healing and type of mass and volume gain in these fault rocks.
3. The 3D geometries and spatial distribution of the different tectonite types (= fault architecture) are time- and scale-dependent (Fig. 10).

With regard to (1), generally fracturing is controlled by the material constants (μ , C) within a given stress field (e.g. Cox, 2005; see also, e.g., modelling in Hooker & Fisher, 2021). Depending on those relations and the stress state, shear fractures, extensional fractures and mixed fractures will dominate (fig. 3 in Cox, 2005). The local porosity and the precipitated cements have a direct feedback on the strength evolution of the associated fault rocks and therefore also on the next fracturing event.

With regard to (2), an important parameter in such an active hydrothermal system is the deformation-induced location of dilatation, i.e. of increasing volumetric strain. The chemical analyses of the different tectonites indicate a substantial mass gain, mainly in

SiO₂ (see also the dominant quartz cements; Figs 5, 6). The maximum gain is ~120 % in the cockade-bearing tectonites and ~50 % (40–60 %) in the cataclasites (Fig. 9). In addition, the still open high porosity adds even more to the volumetric strain of the cockade-bearing tectonites. Due to the similar density of the cataclasites and the added masses, we can state that the mass gain must be directly proportional to a volume gain. This added volume developed during fracturing of the brittle tectonites (Figs 9, 10). Hence locations with substantial increase in volumetric strain indicate where permeability and therefore fluid flux occurred within the large-scale fault architecture prior to clogging by cementation (Fig. 10). The largest volume/mass gain occurs in large open fracture on linkage zones, which often host cockade-bearing tectonites (Fig. 10). In contrast, cataclastic flow during shearing is related to much lower added volumes. Here, the moderate fluid volumes in combination with the deformation-induced small grain sizes promote pressure solution and reaction/precipitation processes (Fig. 6). The quantified moderate SiO₂ mass gain indicates that cataclastic flow produces a lower porosity and a lower amount of mineral precipitation compared to the cockade-bearing structures. Despite still open pore spaces between 5 and 15 % (see Egli *et al.* 2018), cataclasites underwent dominant reaction healing (Fig. 10; see also Gratier *et al.* 2003). Such healing imposes a gain in fault rock strength, which controls type and degree of deformational overprint during the next deformation episode (Fig. 10). The cyclical interaction between brittle deformation and healing shows the dynamics of the maximum strength inside such fault zones. The schematic summary of the presented field data indicates a cyclical behaviour including different speeds and different time intervals (Fig. 10).

With regard to (3), An additional important aspect of the comparison between the different tectonites in this study is their spatial relationships within the fault architecture. One aspect of the spatial relationship is related to the different scales (Fig. 10). The sizes of high- and low-strain domains vary, which can be well shown by comparing large-scale drone images (Fig. 4a), local drone images (Fig. 4b), outcrops (Fig. 5a) and thin-sections (Fig. 10a, b). Another aspect is the geometry of different deformation structures developing with time at different locations (Fig. 4). The cockade-bearing tectonites represent small areas in fault linkage zones of fractures or cataclasites. In the presented medium-scale example in Fig. 4b, most of the fractures are oriented at a ~45° angle with respect to the major deformation zone. The fractures and cockade-bearing tectonites are in a primary orientation parallel to σ_1 . This is supported by the youngest preserved open fracture generation. However, at locations other than the mapping site, cockade-bearing tectonites sometimes show additional deformational overprint. Most obvious are evidences for multiple stages of overprinting, as for example demonstrated by the occurrence of cataclasites within cataclasites (Figs 6a, 10; Hofmann *et al.* 2004; Belgrano *et al.* 2016). Such overprinting relationships are found at all scales ranging from km down to mm.

In summary, the dilatant linkage zones are preferential sites for high volume/mass gain and, therefore, also for enhanced fluid flow. Shear fractures with low volume gain being oriented sub-parallel to the main fault boundaries may be mechanically weak over long time intervals, and therefore will most likely be reactivated. This repeating deformation produces highly comminuted cataclasites or gouges (Fig. 10). In this respect, grain-size reduction processes are inversely proportional to a mass/volume gain. Future studies on comminution of cataclasites should include more detailed geometric characterizations of fault zone architecture in order to

address the different processes of particle size reduction. Potential microstructural relationships may allow for a better differentiation between comminution of a single, fast-rate, seismic high-strain event and comminution during multiple repeating slow-rate (aseismic) and low-strain events. In this context, the well-investigated role of healing (and related mechanical strengthening) strongly depends on the position inside any fault zone in dependence of the scale investigated.

6.d. Relevance for hydrothermal systems and regional fault evolution

In terms of the regional geological relevance, the tube-like structures of cockade-bearing tectonites and cataclastic bands of the GBF are overprinting a pre-existing crustal-scale ductile shear zone (e.g. Wehrens *et al.* 2016, 2017; Herwegh *et al.* 2020). Primarily the change from ductile-dominated shearing along several mylonitic strands to the much more localized brittle GBF relates to a change in deformation mechanisms and their interplay with fluids during progressive exhumation-induced cooling (e.g. Herwegh *et al.* 2020). With embrittlement and associated increase in volumetric strain within the studied fault rocks, enhanced vertical fluid flow allows mass and heat transfer since at least 3.4 Ma (Hofmann *et al.* 2004). In particular, the cockade-bearing tectonites represent the first-order structures for such enhanced flow properties, owing to their enhanced open porosity. In cataclasites, by contrast, small-sized pores are more prone to earlier clogging by cementation. Nonetheless, their mutual geometric and mechanical interaction is necessary to maintain crustal-scale hydrothermal fluid circulation. Based on low-temperature apatite thermochronology, Berger *et al.* (2022) unravelled stages of variable fluid activity along individual fault strands in time. The activity of such different strands of the recent geothermal systems supports the cyclical and overprinting relationships in the different fault rocks observed in the current study (Fig. 10). Moreover, the currently active hydrothermal system gives some insights into the time frame of such hydrothermal systems. The combination of water chemistry and fluid-flow modelling indicates a duration in the range of 30 000 years between infiltration and discharge of the initial meteoric water (Waber *et al.* 2017; Diamond *et al.* 2018). Isotope data of the hydrothermal system indicate an activity over at least the last 3.4 Ma (Hofmann *et al.* 2004), which is two orders of magnitude longer than estimated for the aforementioned individual 30 ka fluid cycle. Both the investigated different exhumed fault rocks and the active hydrothermal system illustrate the changing interplay between embrittlement, fluid flux and precipitation. In this light, hydrothermal fluid flux can be dynamically preserved over millions of years along the same fault structures, although individual fluid pathways locally change in space with time (Fig. 10).

7. Conclusion

The investigated GBF consists of fault segments which contain three main tectonite types: cockade-bearing tectonites, fault gouges and cataclasites. Their mechanical behaviour is based on interactions between comminution, grain growth and healing processes. The latter occurs via mineral precipitation, as manifested by gaining of mass and locally also of volume (mainly in extensional linkage zones of the strike-slip fault system). The increase of masses develops progressively from gouges over cataclasites to cockade-bearing tectonites. In this sequence also, volumetric strain evolves. In terms of a fault's architecture, the highest

volumetric strain occurs in dilational linkage zones of the GBF, which are also the dominant locations of appearance of the cockade-bearing tectonites (Berger & Herwegh, 2019; Figs 3, 9). The increasing volume is related to high fracture porosity. This allows locally high fluid/rock ratios and precipitation processes, which are most pronounced in the cockade-bearing tectonites. Contrastingly the cataclasites show lower amounts of cements, which in the case of the fault gouges are only very minor. This may be related to a higher shear component compared to the cockade-bearing tectonite, since simple shear allows only minor local volume gain, in contrast to mode one fracturing. The differences in cementation between cataclasites and gouges are attributed to differences in the solubilities and stabilities of minerals at the different crustal levels of the active fault structures. On a long-term view, the precursor local frictional behaviour and subsequent precipitation influence the strength of the fault rock at a peculiar stage of fault activity and therefore also the episodic locking/reactivation of specific fault strands. Such sequences demonstrate the importance of the understanding of the fault architecture for fault rocks throughout all scales (e.g. Shipton *et al.* 2005; Caine *et al.* 2010; Masoch *et al.* 2019; Holdsworth *et al.* 2020).

Supplementary material. To view supplementary material for this article, please visit <https://doi.org/10.1017/S0016756822000218>

Acknowledgements. We thank F. Nyffenegger for the careful sieving. D. Egli and T. Belgrano are acknowledged for fruitful discussions about the GBF and their enthusiastic support during sampling. H. Stünitz gave input on an earlier version of the manuscript. This project is part of the NRP70 programme during which drilling was funded by the Swiss National Science Foundation (grant no. SNF-153889). We thank the three anonymous reviewers and the guest editor O. Lacombe for their helpful and constructive comments.

References

- An L-J and Sammis C (1994) Particle size distribution of cataclastic fault materials from southern California: a 3-D study. *Pure and Applied Geophysics* **143**, 203–27.
- Anderson JL, Osborne RH and Palmer DF (1983) Cataclastic rocks of the San Gabriel fault: an expression of deformation at deeper levels in the San Andreas fault zone. *Tectonophysics* **98**, 209–51.
- Belgrano T, Berger A and Herwegh M (2016) Inherited structural controls on fault geometry, architecture and hydrothermal activity: an example from Grimsel Pass, Switzerland. *Swiss Journal of Geoscience* **109**, 345–64.
- Berger A, Egli D, Glotzbach C, Valla PG, Pettke T and Herwegh M (2022) Apatite low-temperature chronometry and microstructures across a hydrothermally active fault zone. *Chemical Geology* **588**, 120633.
- Berger A and Herwegh M (2019) Seismicity in the upper crust: cockade structures as a paleo-earthquake proxy in hydrothermal systems. *Scientific Reports* **9**, 1–9.
- Berger A, Herwegh M, Schwarz J and Putlitz B (2011) Quantitative analysis of crystal/grain sizes and their distributions in 2D and 3D. *Journal of Structural Geology* **33**, 1751–63.
- Berger A, Mercolli I, Herwegh M and Gnos E (2016) Geological map of the Aar Massif, Tavetsch and Gotthard nappes (1:100000). Wabern, Schweiz: Geological Special Map, 129. Landesgeologie Schweiz.
- Blenkinsop TG (1991) Cataclasis and processes of particle size reduction. *Pure and Applied Geophysics* **136**, 59–86.
- Bos B and Spiers CJ (2000) Effect of phyllosilicates on fluid-assisted healing of gouge-bearing faults. *Earth and Planetary Science Letters* **184**, 199–210.
- Bruhn RL, Parry WT, Yonkee WA and Thompson T (1994) Fracturing and hydrothermal alteration in normal fault zones. *Pure and Applied Geophysics* **142**, 609–44.
- Caine JS, Bruhn RL and Forster CB (2010) Internal structure, fault rocks, and inferences regarding deformation, fluid flow, and mineralization in the seismogenic Stillwater normal fault, Dixie Valley, Nevada. *Journal of Structural Geology* **32**, 1576–89.
- Caine JS, Evans JP, and Forster CB (1996) Fault zone architecture and permeability structure. *Geology* **24**, 1025–8.
- Carpenter BM, Ikari JM and Marone C (2016) Laboratory observations of time-dependent frictional strengthening and stress relaxation in natural and synthetic fault gouges. *Journal of Geophysical Research – Solid Earth* **121**, 1183–1201. doi: [10.1002/2015JB012136](https://doi.org/10.1002/2015JB012136).
- Chester F, Friedman M and Logan J (1985) Foliated cataclasites. *Tectonophysics* **111**, 139–46.
- Chester FM and Logan JM (1986) Implications for mechanical properties of brittle faults from observations of the Punchbowl fault zone, California. *Pure and Applied Geophysics* **124**, 79–106.
- Chester J, Chester F and Kronenberg A (2005) Fracture surface energy of the Punchbowl fault, San Andreas system. *Nature* **437**, 133–6.
- Cortinovis S, Balsamo F and Storti F (2019) Influence of analytical operating procedures on particle size distributions in carbonate cataclastic rocks. *Journal of Structural Geology* **128**, 103884.
- Cox S, Ikari MJ, MacLeod CJ and Fagereng Å (2021) Frictional characteristics of oceanic transform faults: progressive deformation and alteration controls seismic style. *Geophysical Research Letters* **48**, e2021GL096292.
- Cox SF (2005) Coupling between deformation, fluid pressures and fluid flow in ore-producing hydrothermal environments. *Economic Geology* 100th anniversary vol., 39–75.
- Cox SF (2010) The application of failure mode diagrams for exploring the roles of fluid pressure and stress states in controlling styles of fracture-controlled permeability enhancement in faults and shear zones. *Geofluids* **10**, 217–33.
- Cox SF and Munroe SM (2016) Breccia formation by particle fluidization in fault zones: implications for transitory, rupture-controlled fluid flow regimes in hydrothermal systems. *American Journal of Science* **316**, 241–78.
- Diamond LW, Wanner C and Waber HN (2018) Penetration depth of meteoric water in orogenic geothermal systems. *Geology* **46**, 1063–6.
- Egli D, Baumann R, Küng S, Berger A, Baron L and Herwegh M (2018) Structural characteristics, bulk porosity and evolution of an exhumed long-lived hydrothermal system. *Tectonophysics* **747–748**, 239–58.
- Evans JP and Chester FM (1995) Fluid-rock interaction in faults of the San Andreas system: inferences from San Gabriel fault rock geochemistry and microstructures. *Journal of Geophysical Research – Solid Earth* **100**, 13007–20.
- Evans JP, Forster CB and Goddard JV (1997) Permeability of fault-related rocks, and implications for hydraulic structure of fault zones. *Journal of Structural Geology* **19**, 1393–1404.
- Faulkner DR, Jackson CAL, Lunn RJ, Schliche RW, Shipton Z, Wibberley CAJ and Withjack MO (2010) A review of recent developments concerning the structure, mechanics and fluid flow properties of fault zones. *Journal of Structural Geology* **32**, 1557–75.
- Fossen H and Cavalcante G (2017) Shear zones: a review. *Earth-Science Reviews* **171**, 434–55.
- Frenzel M and Woodcock NH (2014) Cockade breccia: product of mineralisation along dilatational faults. *Journal of Structural Geology* **68**, 194–206. doi: [10.1016/j.jsg.2014.09.001](https://doi.org/10.1016/j.jsg.2014.09.001).
- Grant JA (1986) The isocon diagram: a simple solution to Gresens' equation for metasomatic alteration. *Economic Geology* **81**, 1976–82.
- Grant JA (2005) Isocon analysis: a brief review of the method and applications. *Physics and Chemistry of the Earth* **30**, 997–1004.
- Gratier JP, Favreau P and Renard F (2003) Modeling fluid transfer along California faults when integrating pressure solution crack sealing and compaction processes. *Journal of Geophysical Research – Solid Earth* **108**, 2104–2129.
- Gresens RL (1967) Composition–volume relationships of metasomatism. *Chemical Geology* **2**, 47–65.
- Hadzadeh J and Johnson WK (2003) Estimating local strain due to comminution in experimental cataclastic textures. *Journal of Structural Geology* **25**, 1973–9.
- Haines SH, Kaproth B, Marone C, Saffer D and van der Pluijm B (2013) Shearzones in clay-rich fault gouge: A laboratory study of fabric development and evolution. *Journal of Structural Geology* **51**, 206–25.

- Handy MR, Hirth G and Hovius N** (2007) Continental fault structure and rheology from the frictional-to-viscous transition downward. In *Tectonic Faults: Agents of Change on a Dynamic Earth* (eds MR Handy, G Hirth and N Hovius), pp. 139–182. Cambridge, Massachusetts: MIT Press.
- Hausegger S and Kurz W** (2013) Cataclastic faults along the SEMP fault system (Eastern Alps, Austria): a contribution to fault zone evolution, internal structure and paleo-stresses. *Tectonophysics* **608**, 237–51.
- Heilbronner R and Barrett S** (2014) *Image Analysis in Earth Sciences: Microstructures and Textures of Earth Materials*. Dordrecht: Springer.
- Heilbronner R and Keulen N** (2006) Grain size and grain shape analysis of fault rocks. *Tectonophysics* **427**, 199–216.
- Herwegh M, Kissling E, Baumberger R, Berger A, Wangenheim C, Wehrens P, Glotzbach C and Mock S** (2020) Late stages of continent–continent collision: timing, kinematic evolution and exhumation of the Northern Rim of the Alps. *Earth Science Review* **200**, 102959.
- Hofmann BA, Helfer M, Diamond LW, Villa IM, Frei R and Eikenberg J** (2004) Topography-driven hydrothermal breccia mineralization of Pliocene age at Grimsel Pass, Aar massif, Central Swiss Alps. *Schweizerische Mineralogische und Petrographische Mitteilungen* **84**, 271–302.
- Holdsworth RE, Trice R, Hardman K, McCaffrey KJW., Morton A, Frei D and Rogers S** (2020) The nature and age of basement host rocks and fissure fills in the Lancaster field fractured reservoir, west of Shetland. *Journal of the Geological Society* **177**, 1057–73.
- Hooker JN and Fisher DM** (2021) How cementation and fluid flow influence slip behavior at the subduction interface. *Geology* **49**, 1074–8.
- Jebra M** (1997) Hydrothermal breccias in vein-type ore deposits: a review of mechanisms, morphology and size distribution. *Ore Geology Reviews* **12**, 111–34.
- Kerrich R, Allison I, Barnett RL, Moss S and Starkey J** (1980) Microstructural and chemical transformations accompanying deformation of granite in a shear zone at Mieville, Switzerland. *Contributions to Mineralogy and Petrology* **73**, 221–42.
- Keulen N, Heilbronner R, Stunitz H, Boullier AM and Ito H** (2007) Grain size distributions of fault rocks: a comparison between experimentally and naturally deformed granitoids. *Journal of Structural Geology* **29**, 1282–1300.
- Keulen N, Stünitz H and Heilbronner R** (2008) Healing microstructures of experimental and natural fault gouge. *Journal of Geophysical Research – Solid Earth* **113**, B06205. doi: [10.1029/2007JB005039](https://doi.org/10.1029/2007JB005039).
- Kruhl J** (2013) Fractal-geometry techniques in the quantification of complex rock structures: a special view on scaling regimes, inhomogeneity and anisotropy. *Journal of Structural Geology* **46**, 2–21.
- Laubach SA, Eichhubl P, Hilgers C and Lander RH** (2010) Structural diagenesis. *Journal of Structural Geology* **32**, 1866–72.
- Luther A, Axen G and Selverstone J** (2013) Particle-size distributions of low-angle normal fault breccias: implications for slip mechanisms on weak faults. *Journal of Structural Geology* **55**, 50–61.
- Marquer D** (1989) Transfert de matière et déformation des granitoides. Aspects méthodologiques. *Schweizer Mineralogische und Petrographische Mitteilungen* **69**, 15–35.
- Masoch S, Fondriest M, Preto N, Secco M, and Di Toro G** (2019) Seismic cycle recorded in cockade-bearing faults (Col de Teghime, Alpine Corsica). *Journal of Structural Geology* **129**, 103889.
- Melosh BL, Rowe CD, Gerbi C, Bate CE and Shulman D** (2016) The spin zone: transient mid-crust permeability caused by coseismic brecciation. *Journal of Structural Geology* **87**, 47–63.
- Melosh BL, Rowe CD, Smit L, Groenewald C, Lambert CW and Macey P** (2014) Snap, crackle, pop: dilatational fault breccias record seismic slip below the brittle plastic transition. *Earth and Planetary Science Letters* **403**, 432–45.
- Micklethwaite S** (2009) Mechanisms of faulting and permeability enhancement during epithermal mineralisation: Cracow goldfield, Australia. *Journal of Structural Geology* **31**, 288–300.
- Micklethwaite S and Cox SF** (2004) Fault-segment rupture, aftershock-zone fluid flow, and mineralization. *Geology* **32**, 813–16.
- Molnar L, Tóth T and Schubert F** (2014) Statistical characterization of brittle and semi-brittle fault rocks: a clast geometry approach. *Acta Geodaetica et Geophysica* **49**, 527–50.
- Monzawa N and Otsuki K** (2003) Comminution and fluidization of granular fault materials: implications for fault slip behavior. *Tectonophysics* **367**, 127–43.
- Nakatan M and Scholz CH** (2004) Frictional healing of quartz gouge under hydrothermal conditions: 1. Experimental evidence for solution transfer healing mechanism. *Journal of Geophysical Research – Solid Earth* **109**, B07201. doi: [10.1029/2001JB001522](https://doi.org/10.1029/2001JB001522).
- Niemeijer A, Marone C and Elsworth D** (2010) Frictional strength and strain weakening in simulated fault gouge: competition between geometrical weakening and chemical strengthening. *Journal of Geophysical Research – Solid Earth* **115**, B10207. doi: [10.1029/2009JB000838](https://doi.org/10.1029/2009JB000838).
- Niemeijer AR and Spiers CJ** (2006) Velocity dependence of strength and healing behavior in simulated phyllosilicate-bearing fault gouge. *Tectonophysics* **427**, 231–53.
- Pfeifer H-R, Sanchez A and Degueldre C** (1992) Thermal springs in granitic rocks from the Grimsel Pass (Swiss Alps): the late stage of a hydrothermal system related to Alpine orogeny. In *7th International Symposium on Water–Rock Interaction* (eds YK Kharaka and AS Maest), pp. 1327–31. Rotterdam: Balkema.
- Phillips NJ and Williams R** (2021) To D or not to D? Re-evaluating particle-size distributions in natural and experimental fault rocks. *Earth and Planetary Science Letters* **553**, 116635.
- Rockwell TK, Sisk M, Girty G, Dor O, Wechsler N and Ben-Zion Y** (2009) Chemical and physical characteristics of pulverized Tejon Lookout Granite adjacent to the San Andreas and Garlock faults: implications for earthquake physics. *Pure and Applied Geophysics* **166**, 1725–46.
- Rolland Y, Cox SF and Corsini M** (2009) Constraining deformation stages in brittle–ductile shear zones from combined field mapping and $^{40}\text{Ar}/^{39}\text{Ar}$ dating: the structural evolution of the Grimsel Pass area (Aar Massif, Swiss Alps). *Journal of Structural Geology* **31**, 1377–94.
- Rowe CD and Griffith WA** (2015) Do faults preserve a record of seismic slip?: a second opinion. *Journal of Structural Geology* **78**, 1–26.
- Rowe CD, Lamothe K, Rempe M, Andrews M, Mitchell TM, Di Toro G and White JC** (2019) Earthquake lubrication and healing explained by amorphous nanosilica. *Nature Communications* **10**, 320.
- Sammis CG, King G and Biegel R** (1987) The kinematics of gouge deformation. *Pure and Applied Geophysics* **125**, 777–812.
- Sammis CG, Osborne R, Lawford-Anderson J, Banerdt M and White P** (1986) Self-similar cataclasis in the formation of fault Gouge. *PAGEOPH* **124**, 53–78.
- Schaltegger U** (1990) Post-magmatic resetting of Rb–Sr whole rock ages: a study in the Central Aar Granite (Central Alps, Switzerland). *Geologische Rundschau* **79**, 709–24.
- Schmid S and Handy M** (1991) Towards a genetic classification of fault rocks: geological usage and tectonophysical implications. In *Controversies in Modern Geology* (eds D Müller, J McKenzie and H Weissert), pp. 339–61. London: Academic Press.
- Shao S-M and Zou J-C** (1996) Fractal research of gouge. *Acta Seismologica Sinica* **9**, 485–91.
- Shipton ZK, Evans JP and Thompson LB** (2005) The geometry and thickness of deformation-band fault core and its influence on sealing characteristics of deformation-band fault zones. *AAPG Memoir* **85**, 181–95.
- Sibson R** (1977) Fault rocks and fault mechanisms. *Journal of the Geological Society of London* **133**, 191–213.
- Sibson RH** (1986) Brecciation processes in fault zones: inferences from earthquake rupturing. *Pure and Applied Geophysics* **124**, 159–75.
- Stalder HA** (1964) Petrographische und mineralogische Untersuchungen im Grimselgebiet (Mittleres Aarmassiv). *Schweizerische Mineralogische und Petrographische Mitteilungen* **44**, 188–384.
- Storti F, Billi A and Salvini F** (2003) Particle size distributions in natural carbonate fault rocks: insights for non-self-similar cataclasis. *Earth and Planetary Science Letters* **206**, 173–86.
- Stünitz H, Keulen N, Hirose T and Heilbronner R** (2010) Grain size distribution and microstructures of experimentally sheared granitoid gouge at coseismic slip rates: criteria to distinguish seismic and aseismic faults? *Journal of Structural Geology* **32**, 59–69.

- Tenthorey E and Cox SF** (2006) Cohesive strengthening of fault zones during the interseismic period: an experimental study. *Journal of Geophysical Research – Solid Earth* **111**, B09202. doi: [10.1029/2005JB004122](https://doi.org/10.1029/2005JB004122).
- Tenthorey E, Cox SF and Todd HF** (2003) Evolution of strength recovery and permeability during fluid–rock reaction in experimental fault zones. *Earth and Planetary Science Letters* **206**, 161–72.
- Torabi A and Berg SS** (2011) Scaling of fault attributes: a review. *Marine and Petroleum Geology* **28**, 1444–60.
- Turcotte DL** (1986) Fractals and fragmentation. *Journal of Geophysical Research – Solid Earth* **91**, 1921–6.
- Waber HN, Schneeberger R, Mäder UK and Wanner C** (2017) Constraints on evolution and residence time of geothermal water in granitic rocks at Grimsel (Switzerland). *Procedia Earth and Planetary Science* **17**, 774–7.
- Wanner C, Diamond LW and Alt-Epping P** (2019) Quantification of 3-D thermal anomalies from surface observations of an orogenic geothermal system (Grimsel Pass, Swiss Alps). *Journal of Geophysical Research – Solid Earth* **124**, 10839–54.
- Wechsler N, Allen EE, Rockwell TK, Girty G, Judith S, Chester JS and Ben-Zion Y** (2011) Characterization of pulverized granitoids in a shallow core along the San Andreas Fault, Littlerock, CA. *Geophysical Journal International* **186**, 401–17.
- Wehrens P, Berger A, Peters M, Spillmann T and Herwegh M** (2016) Deformation at the frictional–viscous transition: evidence for cycles of fluid-assisted embrittlement and ductile deformation in the granitoid crust. *Tectonophysics* **693**, 66–84.
- Wehrens PC, Baumberger R, Berger A and Herwegh M** (2017) How is strain localized in a meta-granitoid, mid-crustal basement section? Spatial distribution of deformation in the central Aar massif (Switzerland). *Journal of Structural Geology* **94**, 47–67.
- White S** (1982) Fault rocks of the Moine thrust zone: a guide to their nomenclature. *Textures and Microstructures* **4**, 211–21.
- Williams RT, Rowe CD, Okamoto K, Savage HM and Eves E** (2021) How fault rocks form and evolve in the shallow San Andreas fault. *Geochemistry, Geophysics, Geosystems* **22**, e2021GC010092.
- Wilson B, Dewers T, Reches Z and Brune JN** (2005) Particle size and energetics of gouge from earthquake rupture zones. *Nature* **434**, 749–52.
- Wise D, Dunn D, Engelder J, Geiser P, Hatcher R, Kish S, Odom A and Schamel S** (1984) Fault-related rocks: suggestions for terminology. *Geology* **12**, 391–4.
- Woodcock N and Mort K** (2008) Classification of fault breccias and related fault rocks. *Geological Magazine* **145**, 435–40.